II. PLASMA DYNAMICS

A. PLASMA PHYSICS[*]

Prof. S. C. Brown	C. D. Buntschuh	W. J. Mulligan
Prof. W. P. Allis	S. Frankenthal	J. J. Nolan, Jr.
Prof. D. J. Rose	R. B. Hall	R. J. Papa
Prof. D. R. Whitehouse	J. L. Hirshfield	Judith S. Vaughen
Dr. G. Bekefi	W. R. Kittredge	C. S. Ward
Dr. L. Mower	J. J. McCarthy	S. Yoshikawa

1. ANOMALOUS CONSTRICTION OF LOW-PRESSURE MICROWAVE DISCHARGES IN HYDROGEN

Four empirical laws that govern the behavior of the constricted discharge with variations in absorbed power and magnetic field have been found. Each of the figures in this report illustrates one of these laws.

a. Variations with Absorbed Power

In a previous report (1) we presented two figures that show the variations of the electron density (n_-) and discharge diameter (d) with the total power absorbed in the microwave cavity (P_{abs}). The power absorbed in the discharge alone (P_g) can be separated from the total absorbed power by making use of the fact that the presence of the discharge in the cavity never shifts the empty-cavity resonance more than 0.8 per cent (2). Figure II-1 shows the results of an experiment performed at a fixed magnetic field and gas pressure. In this figure f_r is the resonant frequency of the cavity plus discharge; f_e is the resonant frequency of the empty cavity; and R_o is the empty-cavity standing-wave ratio. It is seen that d varies in the same way with P_g and P_{abs}, namely

$$\frac{d}{P_g^{1/2}} = \text{constant} \tag{1}$$

independent of P_g. The value of the constant increases slightly with decreasing magnetic field (3).

It was also observed that for a fixed magnetic field

$$dn_- = \text{constant} \tag{2}$$

independent of P_g. This is shown in Fig. II-2, and, again, it is seen that the constant increases with decreasing magnetic field. Thus, combining Eqs. 1 and 2, we have
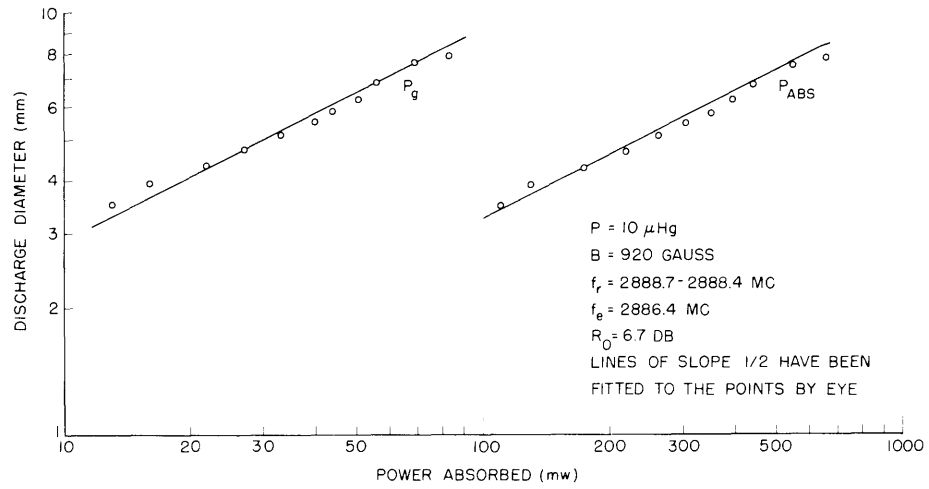

5

Fig. II-1. Discharge diameter versus P_{abs} and P_g.
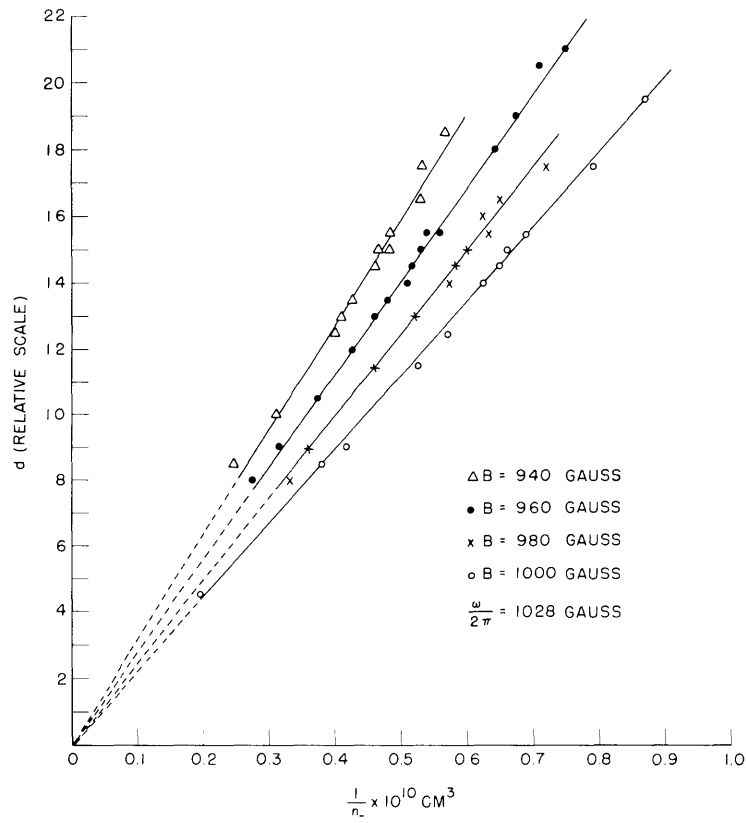
Fig. II-2. Discharge diameter versus reciprocal of electron density for constant $(\omega-\omega_b)$.
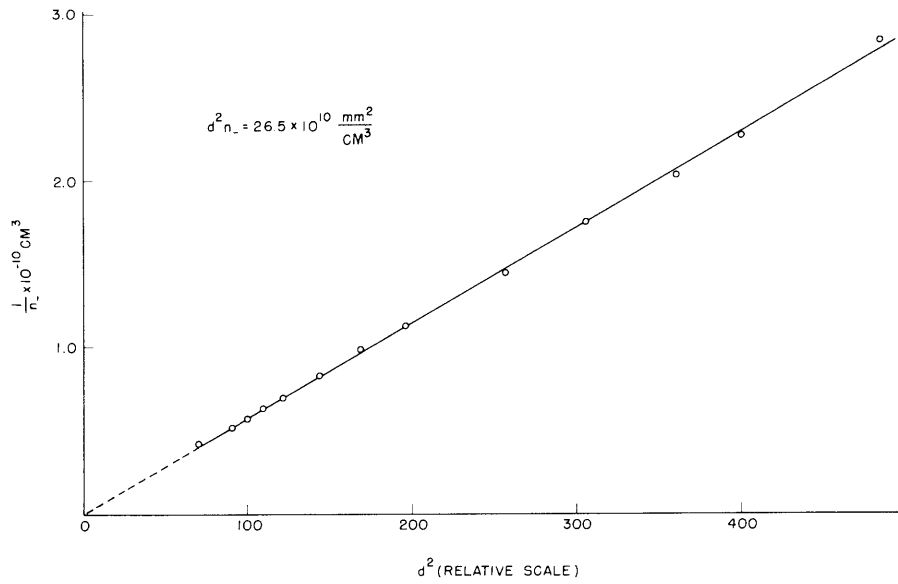
6

$$d^2 n_- = 26.5 \times 10^{10} \ \frac{mm^2}{CM^3}$$

$\frac{1}{n_-} \times 10^{-10} \ CM^3$

d^2 (RELATIVE SCALE)

Fig. II-3. Reciprocal of electron density versus discharge diameter squared for constant P_g.
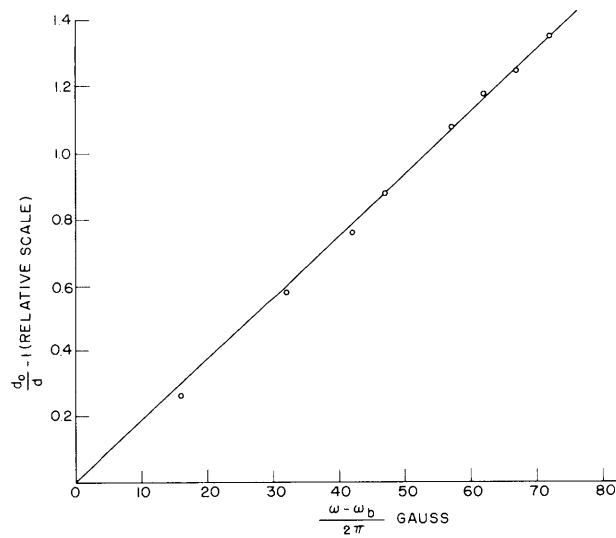
$\frac{d_o}{d} - 1$ (RELATIVE SCALE)

$\frac{\omega - \omega_b}{2\pi}$ GAUSS

Fig. II-4. $(d_o - 1)/d$ versus $(\omega - \omega_b)$ for constant P_g.

7

$$\frac{d^2 n_-}{P_g^{1/2}} = \text{constant} \tag{3}$$

independent of P_g.

b. Variations with Magnetic Field

Figures II-3 and II-4 show the results of a typical experiment when the magnetic field is varied and P_g is held fixed. Figure II-3 shows that

$$d^2 n_- = \text{constant} \tag{4}$$

independent of the magnetic field, and hence Eq. 3 holds for variations in both the magnetic field and P_g. This equation then states that the total number of electrons in the discharge is a function only of the absorbed power. Figure II-4 shows that

$$\frac{2\pi(d_o - d)}{d(\omega - \omega_b)} = \text{constant} \tag{5}$$

independent of the magnetic field.

The cause of the constriction is still unknown.

C. S. Ward

References

1. C. S. Ward, Anomalous constriction in low-pressure microwave discharges in hydrogen, Quarterly Progress Report No. 53, Research Laboratory of Electronics, M. I. T., April 15, 1959, p. 7.

2. D. J. Rose and S. C. Brown, Methods of measuring the properties of ionized gases at high frequencies. II. Measurement of electric field, J. Appl. Phys. 23, 719-722 (1952).

3. C. S. Ward, op. cit., Fig. II-4, p. 8.

2. RADIOFREQUENCY CONSTRICTED DISCHARGE

With the use of a 7-mc transmitter, constriction of the positive column of a mercury discharge has been observed. Figure II-5 is a schematic diagram of the experimental arrangement used. The parallel metal plates above and below the discharge column provide an electric field which, because of the presence of the plasma, is greatly diminished in the region of the plasma. In the present arrangement the ratio of the electric field outside the plasma to the field inside the plasma is very large because of the large ratio of (ω_p/ω).
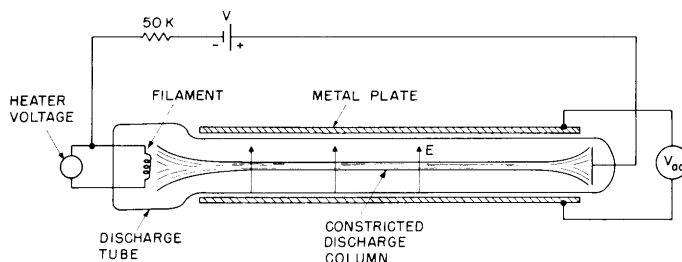
Fig. II-5.   Schematic diagram of constricted mercury discharge.

When the rf voltage is increased in magnitude, the discharge diameter varies from approximately 1 cm to approximately 2-3 mm.   The thickness of the discharge varies both with the applied ac voltage and the dc current passing through the column.   As would be expected, higher currents result in larger thicknesses.   Currents of 60 ma have been constricted by the action of rf fields.

Several other arrangements of the electric-field patterns were tried.   In one arrangement the parallel plate system is replaced by a coaxial electric-field pattern.   A brass tube completely encloses the discharge.   The rf voltage is now applied between the anode of the positive column and the brass tube.   The use of this geometry results in very marked symmetry of the constriction.   This constriction is not now understood.   A partial explanation is being attempted by applying theories on rf confinement (1), whereby a single particle experiences a time-average force that is proportional to the negative gradient of E^2.

R. B. Hall

References

1.   H. A. H. Boot, S. A. Self, and R. B. R. Shersby-Harvie, Containment of a fully ionized plasma by radio frequency fields, J. Electronics and Control, pp. 434-453 (May 1958).

3.   MEASUREMENT OF ELECTRON TEMPERATURE BY CYCLOTRON RADIATION

We have already indicated the possibility of measuring electron temperatures by observations of cyclotron-resonance emission from a plasma (1).   In the previous discussion the plasma was supposed to be situated in free space, the radiation being picked up by a microwave horn.   This scheme has the following disadvantages.   (a) The exact volume of plasma subtended by the horn is unknown and must be determined empirically by comparing it with a plasma of known temperature and similar geometry.   (b) Free space is almost never available to the experimenter, and reflections from surrounding

equipment can alter the opacity of the plasma.

These disadvantages can be overcome if the plasma is situated in a waveguide. The disadvantage here is that the absorption coefficient is not known. However, when the plasma is tenuous and perturbs the waveguide modes slightly, the usual coefficient for a dielectric-filled waveguide can be used. For this situation we have, for the power P radiated from a transparent slab of thickness L into a frequency interval Δf,

$$P = kT\Delta f \frac{a(\theta)\,L}{\left[1-(\lambda/2a)^2\right]^{1/2}}$$

where we have used the θ-dependent absorption coefficient $a(\theta)$ in place of the isotropic one;

$$a(\theta) = \frac{\omega_p^2 \nu}{c} \frac{1}{(\omega-\omega_b)^2 + \nu^2} \frac{1 + \cos^2 \theta}{2}$$

where ω_p, ω_b, and ω are the plasma, cyclotron, and receiver radian frequencies, respectively, and θ is the angle between the wave normal and the magnetic field for plane waves in an infinite plasma. Here, for θ we take the angle that the magnetic field makes with the plane waves into which the unperturbed dominant waveguide mode can be decomposed. That is, $\theta = \cos^{-1}(\lambda/2a)$ for the magnetic field directed transverse to both the waveguide and the electric vector of the waveguide mode.
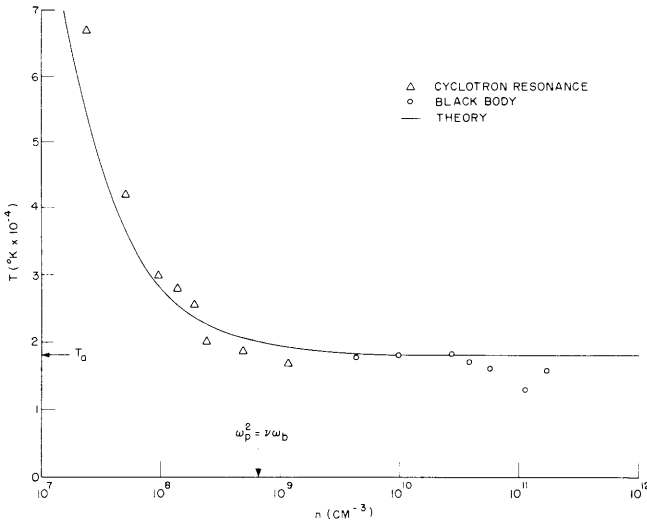
Since our plasma was not in the form of a slab, but of a cylinder, we substitute $L = \pi D^2/4b$, where D is the cylinder diameter, and b is the waveguide height. Here we assume the plasma to be uniform across, and along, the cylinder.

Results of such measurements on a helium glow discharge at $37\,\mu$ Hg are shown in Fig. II-6. Evaluations of data by the cyclotron-resonance method were made by integrating the total power under the resonance line, in order to make the measurement independent of magnetic-field inhomogeneity and other unknown broadening

Fig. II-6. Electron temperature as a function of electron density.

10

mechanisms. The measurements by the black-body method (2) were made by comparison with a standard noise source at the higher electron densities, and with a magnetic field of approximately 0.9 mω/e. We have shown (1) that the plasma radiates essentially as a black body just below cyclotron resonance for $(\omega_p/\omega)^2 > 0.2$.

The theoretical line in Fig. II-6 is obtained by assuming that the electron temperature T in this discharge varies as $T = T_a D_s/D_a$, where T_a is the observed value of T well within the ambipolar diffusion region (see horizontal arrow in the figure), and D_s and D_a are the transitional and ambipolar diffusion coefficients. From results of Allis and Rose (3) for a ratio of 32 for electron to ion mobility, we have constructed the theoretical curve shown in Fig. II-6, in which the value of T_a used is indicated. The vertical arrow on the abscissa indicates the theoretical limit of validity of the cyclotron-resonance method; that is, $(\omega_p^2/\nu\omega_b) = 1$.

J. L. Hirshfield

References

1. J. L. Hirshfield, Quarterly Progress Report No. 54, July 15, 1959, pp. 26-30.

2. J. L. Hirshfield and G. Bekefi, Quarterly Progress Report No. 53, April 15, 1959, pp. 4-7.

3. W. P. Allis and D. J. Rose, Phys. Rev. 93, 84-93 (1954).

4. RADIATION LOSS FROM A WARM PLASMA

As was shown in the last report (1), a cold plasma in a magnetic field with an electron density sufficiently high that the plasma frequency ω_p is greater than the cyclotron frequency ω_b will radiate as a black body at frequencies up to a cutoff frequency in the neighborhood of ω_p. At frequencies higher than this cutoff frequency the plasma is transparent, and the Bremsstrahlung escapes freely. By comparing the magnitude of the black-body radiation with the total Bremsstrahlung (2) it can be seen that the former is often a minor source of radiation loss.

$$P_{bb} = 5.76 \times 10^{-26} \, T \, N^{3/2} \; \text{watts/cm}^2$$

$$P_{Brems} = 5.4 \times 10^{-31} \, T^{1/2} \, N^2 \, Z^2 \; \text{watts/cm}^3$$

where T is the electron temperature in kev, N is the electron density in cm^{-3}, and Z is the atomic number. Thus for a 50-kev deuterium plasma with N = 10^{14} cm^{-3} and with a characteristic dimension L = 10 cm, this comparison gives $P_{Brems}/P_{bb} = 530$. Any means by which the cutoff frequency is raised can increase the radiation loss materially because (from the Rayleigh-Jeans law) the power radiated varies as the cube of

the cutoff frequency. Therefore, in the example just given, if the cutoff frequency is raised from ω_p to $8\omega_p$, then the total radiated power is approximately doubled. It has been suggested (3) that such a means is the emission at frequencies that are harmonics of the cyclotron frequency. These harmonics arise when an energetic electron has its instantaneous radiation pattern thrown asymmetrically forward in the direction of motion along its orbit.

We shall estimate the effect of these harmonics by comparing the peak intensity of a given harmonic with the corresponding intensity given by the Rayleigh-Jeans law within the same frequency interval. The harmonic intensities will be computed as though the plasma were transparent, and our experience with the fundamental will be used. As long as the value of the harmonic intensity comes out higher than that of the black body, we know that the calculation is incorrect, and hence the energy actually appears at other frequencies and tends to fill in the area under the Rayleigh-Jeans curve between harmonics. We shall assume, on the basis of this argument, that the cutoff frequency moves up to approximately that frequency at which the harmonic intensity first falls below that of the black body. This is roughly the scheme used by Trubnikov (4), and by Beard (5), in recent communications on this subject. Comparisons with their results are made below.

The energy I_n radiated in the nth-harmonic line (6) is proportional to the total energy radiated, I_{tot}:

$$\frac{I_n}{I_{tot}} = 3 \frac{(n+1)\, n^{2n+1}}{(2n+1)!} \left(\frac{v_\perp}{c}\right)^{2n-2} \tag{1}$$

where $v_\perp$ is the component of electron velocity transverse to the magnetic field. This formula is invalid for electron energies higher than approximately 20 kev. We assume, by analogy with the fundamental line in a transparent plasma, that the contribution to an over-all line by those electrons having velocities between v and $v + dv$ is a collision-broadened Lorentzian.

$$\frac{I_n(\omega)}{I_{tot}} = \frac{3}{\pi} \frac{(n+1)\, n^{2n+1}}{(2n+1)!} \left(\frac{v_\perp}{c}\right)^{2n-2} \frac{\nu\, d\omega\, dN}{(\omega-\omega_0)^2 + \nu^2} \tag{2}$$

where dN, the fraction of all electrons within dv, is assumed to be Maxwellian

$$dN = \left(\frac{m}{2\pi kT}\right)^{3/2} e^{-mv^2/2kT}\, 4\pi v^2\, dv \tag{3}$$

and thus $(v_\perp/c)^2 = \frac{2}{3}(v/c)^2$. Here ω_0 is the center frequency of this contribution.

$$\omega_0 = n\omega_b \frac{(1-v^2/c^2)^{1/2}}{\left(1-\frac{1}{3}v^2/c^2\right)^{1/2}} \approx n\omega_b \left(1 - \frac{1}{3}\frac{v^2}{c^2}\right) \tag{4}$$

12

with $\omega_b = eB/m$, and ν the collision frequency. The factor in the numerator of Eq. 4 represents the relativistic mass increase; that in the denominator, the Doppler correction for the guiding center motion. We assume that the radiation is observed at right angles to B, so that first-order Doppler effects are absent.

In order to sum over all dv, we require the integral

$$\mathcal{I}_n = \int_0^\infty \frac{x^{n-1/2} e^{-x} dx}{(x-u)^2 + a^2}$$

where

$$x = \frac{mv^2}{2kT}$$

$$u = \frac{3}{2} \frac{mc^2}{kT}\left(\frac{n\omega_b - \omega}{n\omega_b}\right)$$

$$a = \frac{3}{2} \frac{mc^2}{kT}\left(\frac{\nu}{n\omega_b}\right)$$

We can evaluate $\mathcal{I}_n$ exactly by making the substitution

$$\frac{1}{(x-u)^2 + a^2} = \left(\frac{\pi}{2}\right)^{1/2} \sum_{m=0}^\infty \left(\frac{x^2}{u^2+a^2}\right)^{m/2} T_m^{(1/2)}\left[\frac{u}{(u^2+a^2)^{1/2}}\right]$$

where $T_m^{(1/2)}$ are the Tchebychef polynomials, given by $(z^2-1)^{1/2} T_{m-1}^{(1/2)}(z) = \left(\frac{2}{\pi}\right)^{1/2}$ $\sinh[m \cosh^{-1} z]$. The result is

$$\mathcal{I}_n = \left(\frac{\pi}{2}\right)^{1/2} \sum_{m=0}^\infty \left(\frac{1}{u^2+a^2}\right)^{m/2} T_m^{(1/2)}\left[\frac{u}{(u^2+a^2)^{1/2}}\right] \Gamma\left(m+n+\frac{1}{2}\right)$$

Unfortunately, the slow convergence of the $T_m^{(1/2)}$ makes this representation inconvenient to use. Rather, we capitalize upon the fact that $a \ll 1$, and consider the numerator of the integrand of $\mathcal{I}_n$ as remaining stationary over the range of contribution of the denominator, and thereby approximate

$$\mathcal{I}_n \approx u^{n-1/2} e^{-u} \int_0^\infty \frac{dx}{(x-u)^2 + a^2} = \frac{\pi}{a} u^{n-1/2} e^{-u} \qquad (a \ll u) \qquad (5)$$

This approximation was checked by a numerical integration for $u = n - 1/2 = 10$, and $a = 10^{-2}$: the approximate value was less than 5 per cent higher than the numerical evaluation.

Thus we see that the resulting line has its peak moved to a frequency lower than $n\omega_b$ by the amount

$$\Delta\omega = \frac{2}{3}\left(\frac{kT}{mc^2}\right) n(n-1/2)\,\omega_b; \tag{6}$$

has its amplitude multiplied by the factor

$$S_n = 9\sqrt{\pi}\ 2^{n-1}\left(\frac{n+1}{n}\right)\left(n-1/2\right)^{n-1/2} e^{-(n-1/2)}\left(\frac{mc^2}{kT}\right)\frac{\nu}{\omega_b}$$

over what it would be for $\omega_o = n\omega_b$; and has a long tail extending toward lower frequencies, which shows the influence of the electrons in the Maxwellian tail. In regard to the frequency dependence given by Eq. 5: Beard finds that the emission varies with frequency as

$$\left(\frac{n^2\omega_b^2 - \omega^2}{\omega^2}\right)^{n-1} \exp\left[-\frac{mc^2}{2kT}\ \frac{n^2\omega_b^2 - \omega^2}{3\omega^2}\right]$$

as contrasted with our variation.

The shift in the harmonic peak to lower frequencies given by Eq. 6 places a rough upper limit on the cutoff frequency because higher harmonics are shifted in proportion to $n(n-1/2)$; above this limit the net intensity decreases with frequency. Thus for a 10-kev plasma $\Delta\omega \approx [n(n-1/2)\omega_b]/75$, and the peak in the total intensity comes at approximately $38\,\omega_b$. This limit decreases with T; for a 50-kev plasma (7), the peak comes at approximately $8\omega_b$.

The amplitude modification factor S_n can be compared with the results of Beard, who finds the higher harmonics to be increasingly "suffocated" with increasing harmonic number. Table II-1 gives several values of S_n for a plasma with the characteristics: $N = 10^{15}$ cm^{-3}, T = 10 kev, B = 10 kilogauss.

Table II-1.

n	S_n	n	S_n	n	S_n
2	6.90×10^{-3}	5	1.25	8	1.87×10^3
3	2.68×10^{-2}	6	12.5	9	1.40×10^4
4	0.158	7	149	10	1.19×10^5

Here we have used an electron-ion collision frequency ν deduced from Spitzer's (1) conductivity: $\nu = 5.91 \times 10^{-10}$ N T$^{-3/2}$ sec (N in cm^{-3}, T in kev). The increase in line intensity arises because the $(v_\perp/c)^{2n-2}$ factor in Eq. 1 throws strong weight to the high-velocity electrons in the Maxwellian tail at high n.

We now compare the peaks of the lines with the Rayleigh-Jeans limit $B(\omega) = (kT\omega^2 d\omega)/(4\pi^3 c^2)$ for a plasma of dimension L. Here $I_{tot} = \omega_p^2 \omega_b^2 kT/6\pi c^3$, and

$$R_n = \frac{I_n(\omega)_{max}}{B(\omega)} = \frac{\omega_p^2 L}{\omega_b c} \left(\frac{kT}{mc^2}\right)^{n-2} f_n$$

where

$$f_n = 24\sqrt{\pi} \left(\frac{4}{3}\right)^{n-1} \frac{n^{2n-2}(n+1)}{(2n+1)!} (n-1/2)^{n-1/2} e^{-(n-1/2)}$$

A few values of f_n are given in Table II-2.

Table II-2.

n	f_n	n	f_n	n	f_n
2	2.325	8	7.170×10^4	14	4.769×10^{12}
3	3.943	9	1.046×10^6	15	1.381×10^{14}
4	13.78	10	1.769×10^7	16	4.333×10^{15}
5	76.28	11	3.429×10^8	17	1.465×10^{17}
6	5.874×10^2	12	7.448×10^9	18	5.309×10^{18}
7	5.142×10^3	13	1.797×10^{11}	19	2.054×10^{20}

Now let us compare our results with Trubnikov's example of the solar corona: $B = 10$ gauss, $N = 10^7$ cm^{-3}, $L = 7 \times 10^7$ cm, $T = 100$ ev. He finds that four harmonics are absorbed; our calculation gives $R_3 = 418$, $R_4 = 0.292$, and $R_5 = 3.24 \times 10^{-4}$.

Beard cites the following example in his results: For $\omega = 10\omega_b$, $T = 50$ kev, $N = 10^{14}$ cm^{-3}, and $B = 5000$ gauss, he finds $R_{10} = 10^{-4} L$ (L in cm). We find (7) that $R_{10} = 670 L$. Since the highest frequency at which a peak would occur (were the plasma transparent at that frequency) is, from Eq. 6, at approximately $8\omega_b$, the total cyclotron radiation can only be found by summing contributions from the tails of a number of harmonics higher than the eighth, and comparing this sum with the Rayleigh-Jeans intensity.

The aid of Elizabeth J. Campbell, of the Joint Computing Group, M.I.T., is acknowledged in the computation of Table II-2.

J. L. Hirshfield

References

1. J. L. Hirshfield, Microwave radiation from a plasma in a magnetic field, Quarterly Progress Report No. 54, July 15, 1959, pp. 26-30.

2. R. F. Post, Revs. Modern Phys. 28, 344 (1956).

3. U. E. Kruse, L. Marshall, and J. R. Platt, Astrophys. J. 124, 601-604 (1956).

4. B. A. Trubnikov, Soviet Physics Doklady 3, 136-140 (1958).

5. D. B. Beard, Phys. Fluids 2, 379-389 (1959).

6. H. Rosner, Motions and radiation of a point charge in a uniform and constant external magnetic field, Report AFSWC-TR-58-47, Republic Aviation Corporation, Farmingdale, L.I., New York, 15 Nov. 1958, pp. 146-201.

7. Results of these calculations have been applied to 50-kev plasmas, although formula 1 may be invalid here. This was done for the purpose of comparing our results with Beard's examples.

5. CESIUM PLASMA

It has been suggested (1) that a steady-state plasma of high degree of ionization can be obtained by directing a well-defined beam of cesium atoms at a hot tungsten surface and then confining the ions thus produced by a magnetic field. This method appears to have the advantage over other methods (2, 3) (in which the vessel is completely filled with cesium vapor) that the concentration of neutral atoms can be maintained at low levels, with a subsequent increase in the percentage of ionization.

Here we report preliminary measurements that were made with the tube shown schematically in Fig. II-7. A beam of cesium atoms, issuing from an oven maintained at 250°C, impinges on the hot tungsten plate A (1.4 cm^2 in area), whose temperature can be raised to 2400°K. An axial dc magnetic field of approximately 1200 gauss reduces the diffusion loss of the thermal ions to the radial walls of the glass container. The ions are collected by electrode B, which is held negative with respect to A. Electrode B can also be heated, and thus provide electrons for space-charge neutralization of the ion beam. A cold trap kept at -70°C greatly diminishes the vapor pressure of cesium in the right-hand section of the tube. The tube was pumped continuously. With the cesium oven inoperative, the pressure, as measured by an ionization gauge several feet away from the experimental tube, was 5×10^{-8} mm Hg. With the cesium beam turned on, the pressure was 10^{-5} mm Hg.

Figure II-8 shows a plot of the positive ion current collected by the cold electrode B as a function of the heating current of electrode A for a 500-volt potential between A and B. The temperature of electrode A was estimated from the measured electric power input and from the known variation of the resistivity of clean tungsten with temperature. The second abscissa of Fig. II-8 gives this temperature. No ion emission was
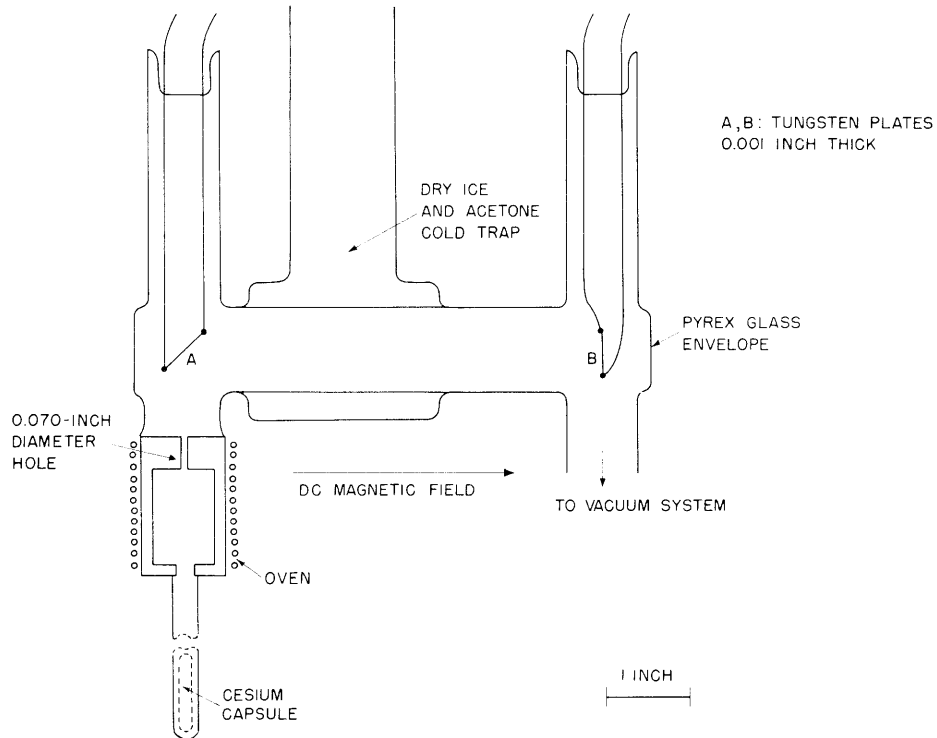
Fig. II-7. Schematic diagram of the cesium tube.

found below approximately 1500°K because here the cesium-coated tungsten has a lower
work function than the ionization potential of cesium. As the temperature increases,
the surface begins to clean up with a subsequent rapid increase of ion emission. Even
at the highest temperatures attained with the present tube, the ion emission does not
show the signs of saturation that are expected to occur when all available ions that are
produced at A are collected at B. Figure II-9 shows a plot of the ion current as a
function of voltage applied between A and B for an electrode A temperature of 1700°K,
and for a magnetic field of 1200 gauss. The shape of this curve is characteristic of all
other measurements that were made at different temperatures of electrode A. For
sufficiently high voltages the ion current is essentially constant; below 100 volts the
current begins to fall off with decreasing voltage.

No absolute measurements of the charge concentration have been made thus far. A
determination of the ion concentration from the current-voltage characteristic requires
a knowledge of the drift velocity of the ion as a function of the applied field. The drift
velocity is not known. However, the magnitude of the density can be taken to lie within
two well-defined limits. The maximum ion current attained in this tube was 3.5 mamp
for a tube voltage of 100 volts. The drift velocity of the ion cannot exceed that associated
with a voltage drop of 100 volts; hence we set a lower limit of 2×10^{10} cm^{-3} for the
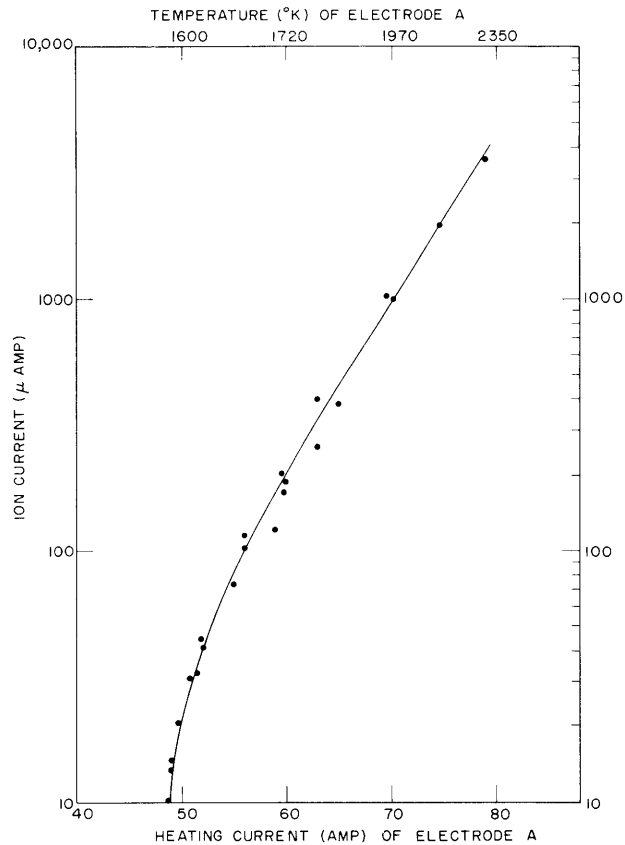
Fig. II-8. Ion current as a function of the electrode heating current and temperature. (Magnetic field, approximately 1200 gauss.)
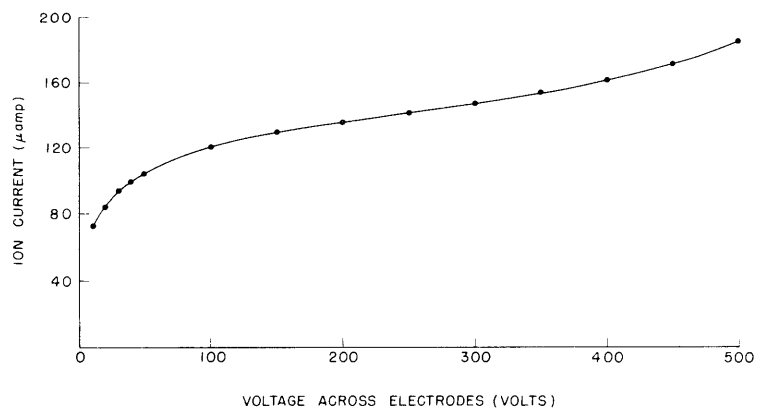

Fig. II-9. Current-voltage characteristic of the cesium tube. (Heater current, 60 amp; heater temperature, 1700° K; magnetic field, 1200 gauss.)

ion density. With the assumption that the ion has a kinetic energy given by the temper-
ature of the hot electrode (2400°K), we obtain an upper limit of 3×10^{11} cm^{-3} for the
density. An idealized calculation, in which it is assumed that (a) every cesium atom is
ionized, (b) the ion drifts down the tube at a velocity corresponding to that of its thermal
energy, and (c) no ions are lost by diffusion or recombination, leads to a saturation
value for the ion density of approximately 10^{12} cm^{-3}. This calculation was made for
an effusion of cesium atoms from a channel, 0.070 inch in diameter and 0.4 inch long,
in an oven maintained at 250°C. The emitting hole was approximately 1 inch away from
the tungsten target.

The estimated high ion density suggests the presence of a large sheath close to elec-
trode B, where most of the voltage drop takes place. Since the electric fields near
electrode A are expected to be correspondingly small, electrons (produced by therm-
ionic emission) can diffuse almost throughout the entire region of the tube between the
two electrodes. These electrons provide the necessary space-charge neutralization of
the ion beam. In this region we expect the value for the ion density to be closer to that
calculated for the upper limit (3×10^{11} cm^{-3}), which is associated with ions drifting at
their thermal velocities. For a vapor pressure of 10^{-5} mm Hg for cesium, the degree
of ionization is, then, approximately 50 per cent.

Work continues toward an absolute determination of the charge particle density with
the use of microwave techniques.

G. Bekefi, R. B. Hall

References

1. Suggestion made by Dr. N. Rynn at the AEC Sherwood Program Microwave
Meeting, M.I.T., June 4-5, 1959.

2. G. M. Grover, D. J. Roehling, and E. W. Salmi, J. Appl. Phys. 29, 1611
(1958).

3. V. C. Wilson, J. Appl. Phys. 30, 475 (1959).

6. NORMAL WAVE SURFACES IN A PLASMA IN A MAGNETIC FIELD

In Quarterly Progress Report No. 54, pages 5-14, normal wave surfaces were
deduced for the propagation of plane waves through a plasma in the presence of a mag-
netic field. In that report it was assumed that there are (a) no density gradients; (b) no
collisions; and (c) no thermal motions. In this report the restriction on thermal motions
is removed, but the motions of the ions are neglected.

The dispersion equation has been obtained by Sitenko and Stepanov (1) and also by
Bernstein (2). It has recently been re-derived by S. J. Buchsbaum (3). The Boltzmann
equation is linearized by a perturbation technique. Assuming small deviations, f, from

19

the equilibrium distribution f_o, we obtain, by neglecting products of small quantities,

$$\frac{\partial f}{\partial t} + \vec{v} \cdot \vec{\nabla}_r f + \frac{e}{m}(\vec{E}_o + \vec{v} \times \vec{B}_o) \cdot \vec{\nabla}_v f + \frac{e}{m}(\vec{E}_1 + \vec{v} \times \vec{B}_1) \cdot \vec{\nabla}_v f_o = -\nu_c f$$

where

$$f_o = n_o \left(\frac{m}{2\pi eT}\right)^{3/2} e^{-mv^2/2eT}$$

with n_o, the equilibrium electron density, and T in electron-volts. Since f_o is iso-tropic in velocity, we have

$$\frac{e}{m}\vec{v} \times \vec{B}_1 \cdot \vec{\nabla}_v f_o = \frac{e}{m}(\vec{\nabla}_v f_o \times \vec{v}) \cdot \vec{B}_1 = 0$$

Because collisions are neglected ($\nu_c = 0$) and there are no dc electric fields, we obtain

$$\frac{\partial f}{\partial t} + \vec{v} \cdot \vec{\nabla}_r f + \frac{e}{m}\vec{E}_1 \cdot \vec{\nabla}_v f_o + \frac{e}{m}\vec{B}_o \cdot \vec{v} \times \vec{\nabla}_v f = 0 \tag{1}$$

Assume that

$$\vec{E}_1(r, t) = \vec{E}(k, \omega) e^{j(\vec{k} \cdot \vec{r} - \omega t)} \tag{2}$$

$$f(r, v, t) = f(v, k, \omega) e^{j(\vec{k} \cdot \vec{r} - \omega t)} \tag{3}$$

and $\vec{B}_o = \vec{B}$.

Substituting Eqs. 2 and 3 in Eq. 1 gives

$$j(\vec{k} \cdot \vec{v} - \omega) f + \frac{e}{m}\vec{E} \cdot \vec{\nabla}_v f_o - \omega_B \frac{\partial f}{\partial \phi} = 0 \tag{4}$$

where $\omega_B = eB/m$, and ϕ is the azimuthal angle in the velocity space. The z-axis is directed along the magnetic field B, and the angle θ is the angle between $\vec{B}$ and $\vec{k}$.

Integrating Eq. 4 gives

$$f = \frac{e}{m\omega_B}\frac{\vec{E}}{P} \cdot \int_0^\phi \vec{\nabla}_v f_o P\, d\phi + \left(\frac{e}{m\omega_B}\right)\frac{\vec{C}}{P} \cdot \vec{E} \tag{5}$$

where the integrating factor

$$P = \exp\left[-j/\omega_B \int_0^\phi (\vec{k} \cdot \vec{v} - \omega)\, d\phi\right]$$

The constant of integration $\vec{C}$ is determined from the condition of periodicity,

$f(\phi+2\pi) = f(\phi)$. Hence

$$\vec{C} = \frac{\int_0^{2\pi} \vec{\nabla}_v f_o \frac{1}{P} \, d\phi}{\left[1 - \exp\left\{\frac{j}{\omega_B} \int_0^{2\pi} (\vec{k} \cdot \vec{v} - \omega) \, d\phi\right\}\right]} \tag{6}$$

The current $\vec{J}$ is given by

$$\vec{J} = e \int \vec{v} f d^3 v = \vec{\sigma} \cdot \vec{E} \tag{7}$$

Defining the dielectric tensor $\vec{K}$ as

$$\vec{K} = \vec{1} + \vec{\sigma}/j\omega\epsilon_o \tag{8}$$

we obtain

$$K_{i\ell} = \delta_{i\ell} + \frac{je^2}{m \omega_b \omega \epsilon_o} \int \frac{v_i}{P}\left[\int_0^{\phi} \frac{\partial f_o}{\partial v_\ell} p \, d\phi + C_\ell\right] d^3 v \tag{9}$$

Expression 9 for $K_{i\ell}$ has been worked out by Buchsbaum (3). He found that the solutions for the dielectric tensor $\vec{K}$ can be expressed in terms of sums of integrals of Bessel functions. For low temperatures $\left[(k^2 eT)/\left(m\omega_B^2\right) \ll 1\right]$ the Bessel functions can be expanded in a series, and thus relatively simple expressions (1) for the components of $\vec{K}$ will be obtained:

$$\left.\begin{aligned}
K_{11} &= 1 - \frac{a^2}{1 - \beta^2} - \epsilon n^2 \left[\frac{1 + 3\beta^2}{(1-\beta^2)^3} \zeta^2 + \frac{3}{(1-\beta^2)(1-4\beta^2)} \xi^2\right] \\[2ex]
K_{22} &= 1 - \frac{a^2}{1 - \beta^2} - \epsilon n^2 \left[\frac{1 + 3\beta^2}{(1-\beta^2)^3} \zeta^2 + \frac{1 + 8\beta^2}{(1-\beta^2)(1-4\beta^2)} \xi^2\right] \\[2ex]
K_{33} &= 1 - a^2 - \epsilon n^2 \left[3\zeta^2 + \frac{1}{1-\beta^2} \xi^2\right] \\[2ex]
K_{12} &= -K_{21} = \frac{-ja^2\beta}{1 - \beta^2} - j\epsilon n^2\beta \left[\frac{3 + \beta^2}{(1-\beta^2)^3} \zeta^2 + \frac{6}{(1-\beta^2)(1-4\beta^2)} \xi^2\right] \\[2ex]
K_{13} &= K_{31} = \frac{-2\epsilon n^2 \xi\zeta}{(1-\beta^2)^2} \\[2ex]
K_{23} &= -K_{32} = j\epsilon n^2\beta \frac{3 - \beta^2}{(1-\beta^2)^3} \xi\zeta
\end{aligned}\right\} \tag{10}$$

(II. PLASMA DYNAMICS)

where

$$a^2 = \frac{n_o e^2}{m\epsilon_o \omega^2}; \quad \beta^2 = \frac{\omega_B^2}{\omega^2} = \frac{e^2 B^2}{m^2 \omega^2}; \quad \epsilon = \frac{eT}{mc^2} \quad a^2 = \left(\frac{av_p}{c}\right)^2$$

with $\xi = \sin\theta$, and $\zeta = \cos\theta$.

These expressions for the components of $\overleftrightarrow{K}$ must now be used in

$$\vec{n} \times (\vec{n} \times \vec{E}) + \overleftrightarrow{K} \cdot \vec{E} = 0 \tag{11}$$

(which is Eq. 8 of Quarterly Progress Report No. 54, p. 6).

The dispersion equation is obtained by setting the determinant of Eq. 11 equal to zero. The result is

$$A^* n^4 - B^* n^2 + C^* = 0 \tag{12}$$

where

$$\left.\begin{aligned}
A^* &= K_{11}\xi^2 + K_{33}\zeta^2 + 2K_{13}\xi\zeta \\[1em]
B^* &= 2(K_{22}K_{13}-K_{12}K_{23})\zeta\xi + (K_{22}K_{33}+K_{23}^2)\zeta^2 - K_{13}^2 \\[1em]
&\quad + K_{11}K_{22} + (K_{11}K_{22}+K_{12}^2)\xi^2 \\[1em]
C^* &= |K_{i\ell}|
\end{aligned}\right\} \tag{13}$$

Substituting expressions 10 in expressions 13, and then using Eq. 12, enables us to write the dispersion equation for low temperatures:

$$-\epsilon a n^6 + (A+b\epsilon)n^4 - (B+c\epsilon)n^2 + C = 0 \tag{14}$$

where

$$\left.\begin{aligned}
A &= (1-\beta^2)(1-a^2) - \beta^2 a^2 \xi^2 \\[1em]
B &= 2(1-a^2)(1-a^2-\beta^2) - \beta^2 a^2 \xi^2 \\[1em]
C &= (1-a^2)[(1-a^2)^2 - \beta^2]
\end{aligned}\right\} \tag{15}$$

are the coefficients previously used, and

$$a = 3(1-\beta)\zeta^4 + \frac{6 - 3\beta^2 + \beta^4}{(1-\beta^2)^2}\xi^2\zeta^2 + \frac{3\xi^4}{1 - 4\beta^2}$$

$$b = 2\left[\frac{2(1-a^2+\beta^2) + \beta^2(1-\beta^2)}{(1-\beta^2)^2}\right]\xi^2\zeta^2$$

$$+ (1+\zeta^2)\left[\frac{(1-a^2-\beta^2)\xi^2 - 3\beta^2(2-a^2-\beta^2)\zeta^2}{(1-\beta^2)} + 4\frac{(1-a^2)}{(1-\beta^2)^2}\zeta^2\right]$$

$$\times \left[\frac{3(1+\zeta^2)(1-a^2) + 4(1-a^2+2\beta^2)\xi^2}{1 - 4\beta^2}\right]\xi^2$$

$$c = 2(1-a^2)\frac{[(1+\beta^2)(1-a^2)+2\beta^2]}{(1-\beta^2)^2}\zeta^2 + \frac{(1-a^2-\beta)(1-a^2+\beta)}{(1-\beta^2)}[3\zeta^2(1-\beta^2)+\xi^2]$$

$$+ \left[\frac{4(1-a^2)(1-a^2+2\beta^2)}{1 - 4\beta^2}\right]\xi^2$$

(16)

give the additional terms in the dispersion equation that are attributable to thermal motions. The equation is now bi-cubic, as it ought to be, and yields three double solutions.

For moderate temperatures $\epsilon \ll 1$, so that $A \gg b\epsilon$, and $B \gg c\epsilon$. Thus Eq. 14 can be written approximately
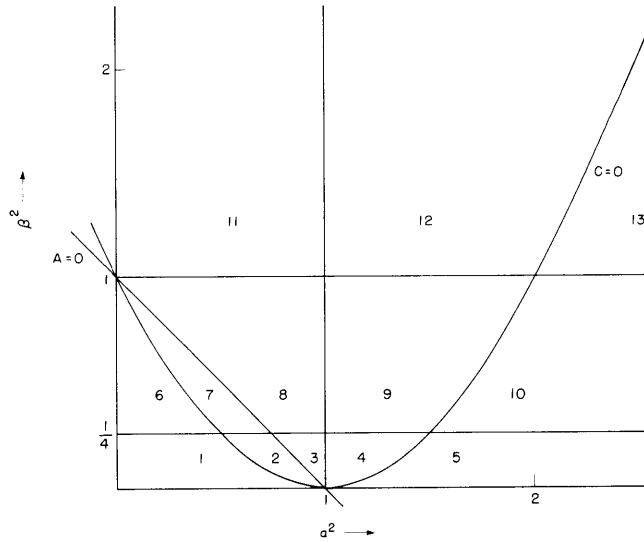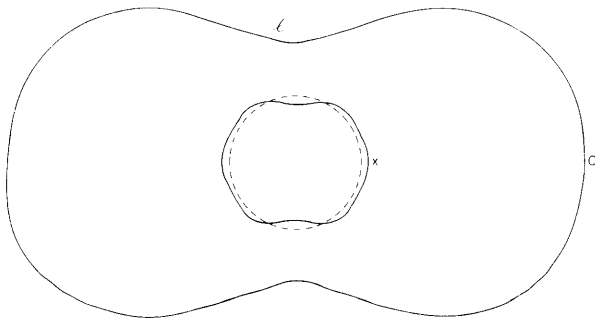

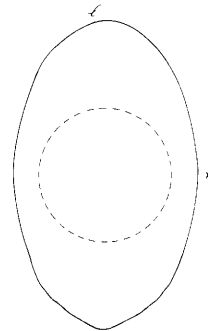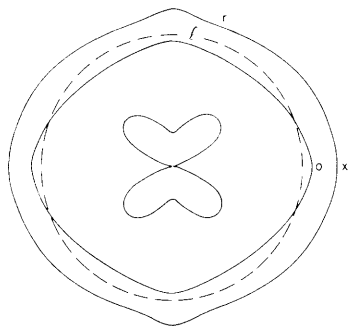Fig. II-10. Plot of β^2 against a^2 showing resonances and cutoffs.
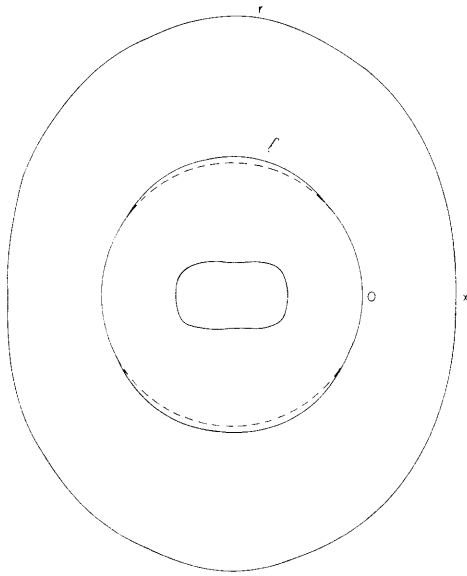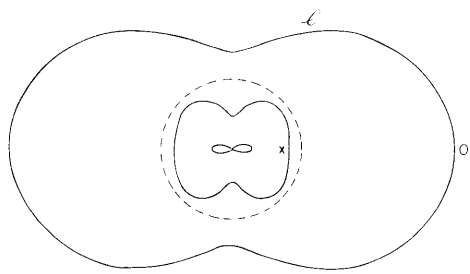
REGION 1
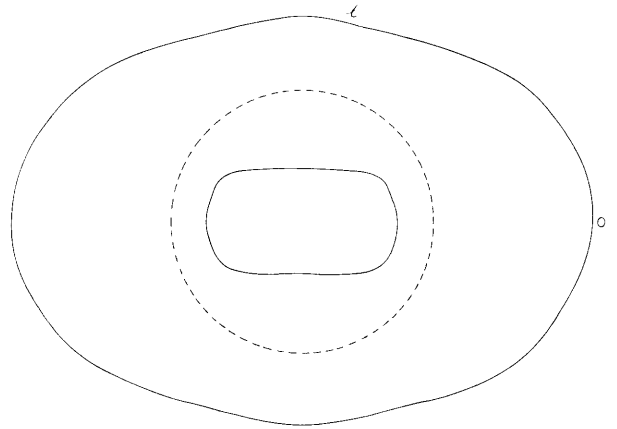
REGION 2

REGION 3

REGION 4

REGION 6
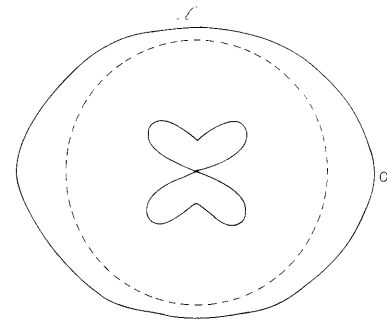
REGION 7
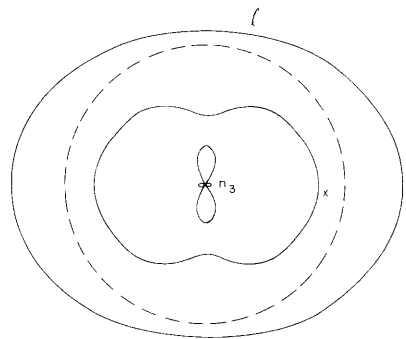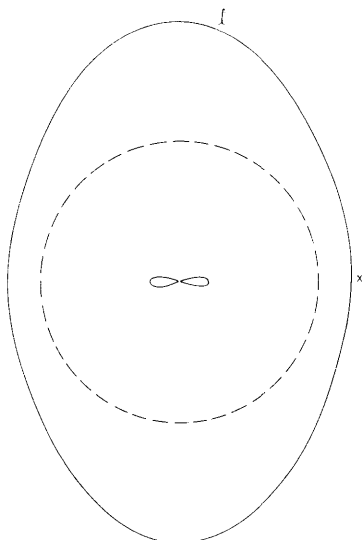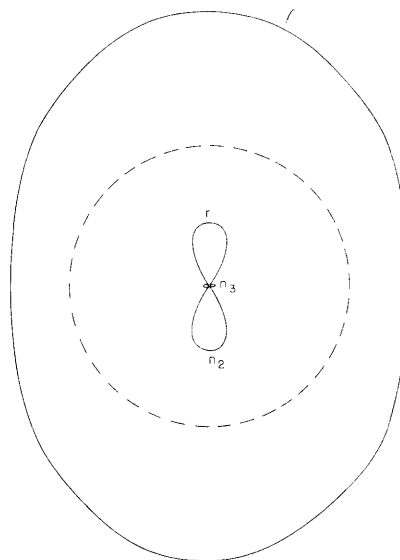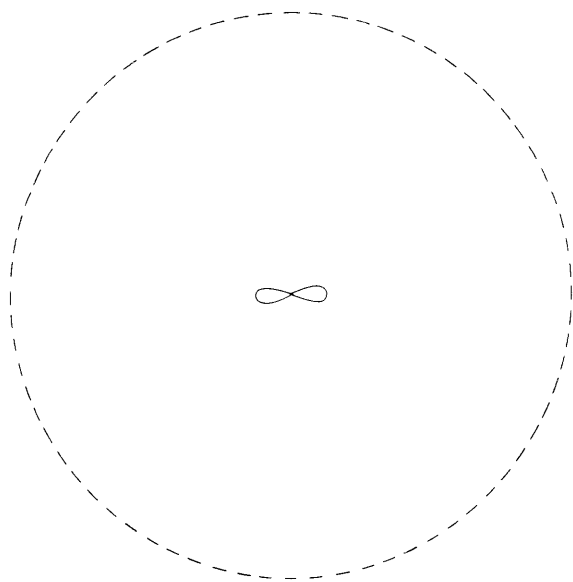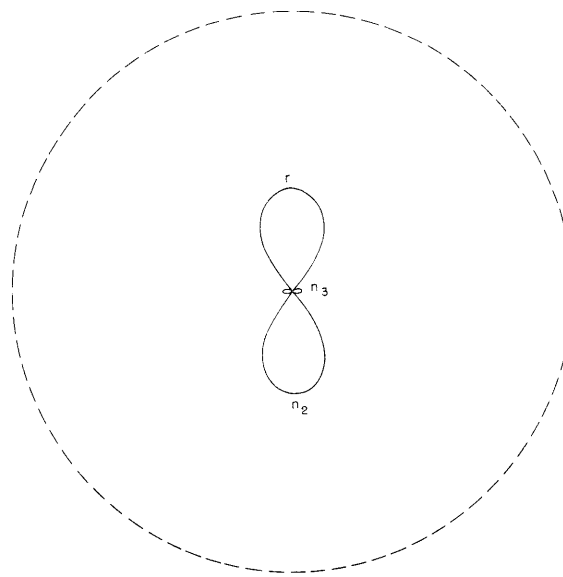
REGION 8

REGION 11

REGION 9

REGION 12

REGION 10

REGION 13

Fig. II-11. Normal wave surfaces in a plasma in a magnetic field.

$$-\epsilon a n^6 + A n^4 - B n^2 + C = 0 \tag{17}$$

For normal n, we may neglect the first term and obtain the dispersion equation, whose solutions are

$$n^2_{1,2} = \frac{B \pm (B^2 - 4AC)^{1/2}}{2A} \tag{18}$$

These solutions give rise to the "fast" waves, whose normal wave surfaces were plotted in the last report. The first quadrant of the β^2 versus α^2 graph was divided into 8 regions by the 3 lines $\alpha^2 = 1$, $\beta^2 = 1$, and $A = 0$, and by the parabola $C = 0$. Wave surfaces exist for 7 of these regions.

There is, however, another solution whose index n is normally large, and whose velocity is of the order of the electron's thermal velocity v_p. These waves will be called "plasma waves" and their index is n_3. This solution can be obtained approximately by neglecting C in Eq. 17. We obtain

$$\epsilon a n^4 - A n^2 + B = 0 \tag{19}$$

whose solution is

$$n^2_{2,3} = \frac{A \pm (A^2 - 4a\epsilon B)^{1/2}}{2\epsilon a} \tag{20}$$

The first quadrant of the β^2 versus α^2 graph is now divided into 13 regions, as shown in Fig. II-10. There is a line now at $\beta^2 = 1/4$. For $\beta^2 < 1/4$, a is positive. For $1/4 < \beta^2 < 1$, the coefficient of the term $\sin^4 \theta$ in a has become negative. For $\beta^2 > 1$, both the coefficients of $\cos^4 \theta$ and $\sin^4 \theta$ in a are negative.

The plasma waves can propagate in some directions for all regions except regions 3, 4, and 5. Only in regions 1 and 2 do plasma waves propagate in all directions. The approximations (Eqs. 18 and 20) are satisfactory when $n^2_3 \gg n^2_1$ and $n^2_3 \gg n^2_2$. This proves not to be the case in region 3.

The cubic equation (Eq. 14) is then solved directly by transforming it into a quadratic in $\sin \theta$, and thus it is rewritten

$$\sin^2 \theta = \frac{-B' \pm (B'^2 - 4A'C')^{1/2}}{2A'} \tag{21}$$

where

$$A' = -\epsilon n^6 \left[\frac{3}{1 - 4\beta^2} + 3(1-\beta^2) - \frac{6 - 3\beta^2 + \beta^4}{(1-\beta^2)^2} \right]$$

$$B' = -\epsilon n^6 \left[-6(1-\beta^2) + \frac{6 - 3\beta^2 + \beta^4}{(1-\beta^2)^2} \right] + n^2 (1-n^2) \alpha^2 \beta^2 \tag{22}$$

$$C' = -\epsilon n^6 [3(1-\beta^2)] + n^4 [(1-\beta^2)(1-\alpha^2)] - n^2 [2(1-\alpha^2)(1-\alpha^2-\beta^2)] + [(1-\alpha^2)\{(1-\alpha^2)^2-\beta^2\}]$$

Figure II-11 shows the wave surfaces for all regions shown in Fig. II-10 where waves exist. As a^2 increases from region 1 to region 2, the normal wave surface for the plasma wave becomes larger, and when it reaches region 3 it joins the normal wave surface for the wave associated with the index of refraction n_2. In region 3, there is no plasma wave. As a^2 increases, the butterfly-shaped wave surface for n_3 in regions 6 and 7 transforms into the oval-shaped wave surface for n_2 in region 8. The plasma-wave surface in region 8 is a horizontal lemniscate, which retains its shape in regions 9 and 10. In region 11, the plasma-wave surface is a four-leafed rose, which becomes a horizontal lemniscate in regions 12 and 13. For all regions, $\epsilon = 10^{-2}$.

<div align="right">W. P. Allis, R. J. Papa</div>

References

1. A. G. Sitenko and K. N. Stepanov, J.E.T.P. (Soviet Physics) $\underline{31}$, 642 (1956).

2. I. B. Bernstein, Phys. Rev. $\underline{109}$, 10 (1959).

3. S. J. Buchsbaum, Section D-27, Microwave conductivity of a hot plasma, Notes on Plasma Dynamics, Summer Session, M.I.T., 1959 (unpublished).

7. NONADIABATIC MOTION OF A CHARGED PARTICLE IN A MIRROR MAGNETIC FIELD

If a charged particle is moving in an axially symmetric magnetic field $\underline{B}$ (Fig. II-12) with appropriate direction at the center, then it is well known that it can be confined for many traversals of a region (1, 2) such as the one between C and D. The result has application in thermonuclear devices and to the Van Allen radiation belt.

The confinement arises from the adiabatic invariance of the magnetic moment M of the particle. Since M is not strictly invariant, for finite Larmor radius $r_b = mv_b/qB$ (with m, the mass, v, the velocity normal to B, and q, the charge), it should vary on
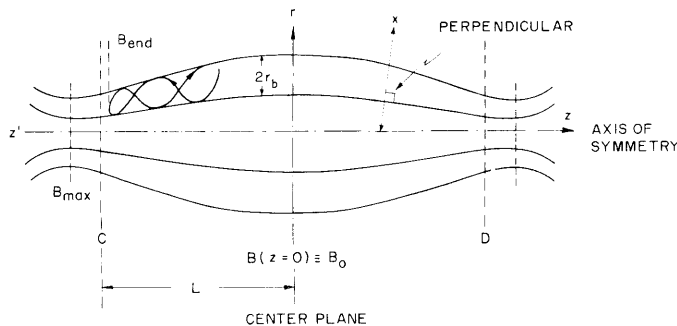

Fig. II-12. Axially symmetric magnetic field (mirror).

successive C-D traverses. Calculations of this effect are reported here.

The Hamiltonian of the charged particle is

$$H = \left[\underline{P}_r^2 + \left(\frac{\underline{P}_\theta}{r} - q\underline{A}_\theta \right)^2 + \underline{P}_z^2 \right] \Big/ 2m \tag{1}$$

where $\underline{P}$ and $\underline{A}$ are the momentum and the vector potential. For a cylindrically symmetric system, $A_r = A_z = \partial/\partial\theta = 0$, and $\nabla \cdot \underline{A} = 0$. Then $\partial H/\partial\theta = 0$, and P_θ is a constant, and hence Eq. 1 can be written

$$H = \frac{1}{2m} \left(P_r^2 + P_z^2 \right) + U(r, z) \tag{2}$$

Equation 2 thus expresses two-dimensional motion in a potential $U(r, z)$. For a large class of orbits encircling the axis, it can be shown (2, 3) that U has the shape of a trough closed at the ends. Then the particle is confined in some C-D region, regardless of the limited excursions of M. Such orbits are not of interest to us, nor is the trivial class of all orbits that close on themselves. The other orbits are interesting to us, for example, orbits in which U has the form of a trough that is pinched in, but open, at the ends. Then by the ergodic hypothesis, the particle should eventually find the opening and escape. Garren and others (2) have numerically calculated such orbits, and tentatively conclude that the particle is permanently confined. However, their calculations ended with too few reflections taken into account.

The present calculation proceeds by expanding the Hamiltonian in powers of r_b/L, where L is a characteristic length, indicated in Fig. II-12, and r_b is taken at the center, $z = 0$. Then in the system of units with $m = q = 1$,

$$H = \frac{1}{2} \left(P_x^2 + P_z^2 \right) + \frac{1}{2}\omega_o^2 x^2 \rho^2 + \text{higher terms} \tag{3}$$

for a mirror field symmetric about $z = 0$. Here, $\rho = B(z)/B(z=0)$ is the "mirror ratio," and ω_o is the cyclotron frequency at the center. The higher-order terms are neglected because the terms that are retained are sufficient to demonstrate the nonadiabatic nature of M. By analogy with the Wentzel-Kramers-Brillouin method, we set

$$x = \frac{\sqrt{2M}}{\rho^{1/2}\omega_o} \cos (\phi + \phi_o)$$

$$\phi = \int_0^t \omega_o \rho \, dt \tag{4}$$

and obtain

$$H = \frac{1}{2} P_z^2 + \rho M [1 + K(x, z, \dot{x}, \dot{z}, t)] \tag{5}$$

Generally, $K \ll 1$ and expresses the change in magnetic moment M. We find that

$$K = \int_0^t \frac{d}{dt} \left[\frac{1}{2} \frac{1}{\rho} \cos^2 (\phi + \phi_0) \right] \frac{d}{dt} \left(\frac{1}{\rho^2} \frac{d\rho}{dt} \right) dt \qquad (6)$$

From Eq. 6, we can show that the maximum change ΔM in the magnetic moment is given by

$$\frac{\Delta M}{M} = \frac{g}{2} \left(\frac{r_b}{L} \right)^2 \left(\frac{B_{end} - B_0}{B_0} \right)^2 \qquad (7)$$

where the quantity g has a value close to unity.

That the variation in magnetic moment is proportional to $(r_b/L)^2$ is verified by the computation of several orbits on the IBM 704 computer. The results are shown in Fig. II-13. In a mirror field with long central section, or in an asymmetric mirror, we would expect the particle to pass the midpoint each time in random phase. Then the
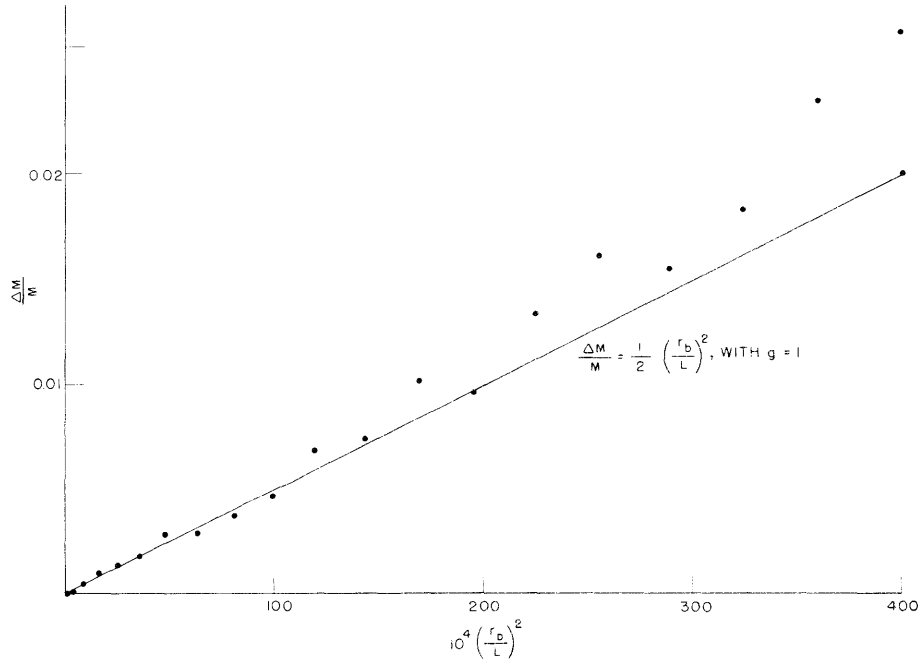

Fig. II-13. Dependence of change of magnetic moment on $\left(\frac{r_b}{L} \right)^2$ for $B_{end} = 2B_0$.

magnetic moment and the end points C and D perform a random walk, and a typical particle will escape from the system after N oscillations, with

$$N = \left(\frac{L}{r_b} \right)^4 \frac{2B_0^2}{g^2 (B_{end} - B_0)^2} \left(1 - \frac{B_{end}}{B_{max}} \right)^2 \qquad (8)$$

Here, B_{end} is the point of initial reflection.

Our calculation also showed that in a completely symmetric analytic field, this first-order perturbation essentially cancels, and hence the next higher term, which is smaller by the factor $(r_b/L)^2$, must be considered. The particle would then be better confined; this fate seems to have befallen the particles traced by Garren (2).

S. Yoshikawa

References

1. L. Spitzer, Jr., Physics of Fully Ionized Gases (Interscience Publishers, Inc., New York, 1956), pp. 7-11.

2. A. Garren, R. J. Riddell, L. Smith, G. Bing, L. R. Henrich, T. G. Northrop, and J. E. Roberts, Individual particle motion and the effect of scattering in an axially symmetric magnetic field, United Nations Peaceful Uses of Atomic Energy, Proc. Second International Conference, Geneva, September 1958, Vol. 31, pp. 65-71 (1958).

3. Thermonuclear Project Semi-Annual Report for Period Ending January 31, 1959, Report ORNL-2693, Oak Ridge National Laboratory, 1959, pp. 18-22.

8. ELECTRIC POLARIZATION OF A CHARGED BEAM IN A MAGNETIC FIELD

This report summarizes a preliminary investigation of the behavior of a beam of charged particles in a magnetic field transverse to the particle motion. The configuration is shown in Fig. II-14, in which 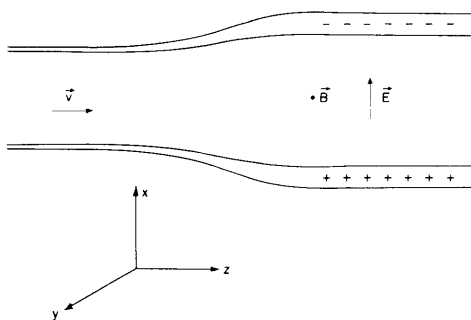a flat beam, consisting of both ions and electrons, moving in the z-direction, is injected across a homogeneous magnetic field $\underline{B}$ (out of the paper in Fig. II-14). The beam is uniform and infinite in the y-direction. The magnetic field causes charges of opposite sign to separate, which gives rise to charged sheaths at both edges of the beam. The electric field $\underline{E}$ arising from these sheaths permits the central part of the beam to continue its motion along the z-direction.

Fig. II-14. Beam polarization in a magnetic field.

In the region where the charged sheaths build up, the fields vary in both the x- and the z-directions. Eventually, the beam is assumed to reach a steady state in which all variations with z disappear. We restrict our attention to this region.

The common assumption that the Larmor radius is small compared with the significant lengths $\left(\frac{E}{\nabla E}\right)$ in the problem is not justified in this case. We cannot, therefore, resort to first-order orbit theory. Rather, we must obtain the charge density in any region by counting the number of particles that go through it and weighting that number

by the time interval that they spend in passing through it.

The equations of motion for a moving charge are:

$$E(x) - v_z B = \frac{m}{q} \frac{dv_x}{dt} \qquad (1)$$

$$v_x B = \frac{m}{q} \frac{dv_y}{dt} \qquad (2)$$

The conservation of energy principle leads to

$$v_x^2 = - \frac{2q}{m} [\phi(x) - \phi(x_o)] - \omega_b^2 (x - x_o)^2 - 2\omega_b v_o (x - x_o) \qquad (3)$$

where $\phi(x)$ is the potential, x_o the position at perigee, v_o the velocity at perigee (see Fig. II-15), and $\omega_b = qB/m$. Given the form of the potential, Eq. 3 yields the x component of the velocity as a function of the position of the particle. Note that the position

Fig. II-15. Typical ion trajectory.

as a function of time can be obtained by integrating the equation

$$dt = \frac{dx}{v_x(x, x_o, v_o)} \qquad (4)$$

with v_x given by Eq. 3. The existence of stable orbits (such as the one in Fig. II-15) depends on the existence of periodic solutions to Eq. 4.
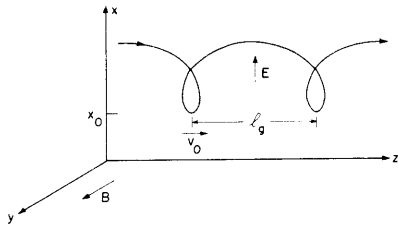
Now we assume that such orbits exist, and pretend that $\phi(x)$ is known. The roots of Eq. 3, with v_x set equal to zero, give perigee x_o and apogee $x_a(x_o, v_o)$ of the orbit. We can then define a gyration period

$$\tau_g = 2 \int_{x_o}^{x_a} \frac{dx}{v_x} \qquad (5)$$

and an average (guiding center) velocity v_g. The latter is obtained from Eq. 1 as

$$v_g = \frac{2}{B \tau_g} \int_{x_o}^{x_a} \frac{E(x)}{v_x} dx \qquad (6)$$

The gyration length ℓ_g (distance from perigee to perigee), is

$$\ell_g = v_g \tau_g = \frac{2}{B} \int_{x_o}^{x_a} \frac{E(x)}{v_x} dx \qquad (7)$$

We now proceed to evaluate the particle density at a point x: First, note that a

particle with perigee parameters x_O and v_O will spend a time interval

$$dt = \frac{2dx}{v_x(x, x_O, v_O)} \tag{8}$$

per gyration in an element of position dx. Thus, the probability of finding it there is

$$\frac{dt}{\tau_g} = \frac{2dx}{\tau_g v_x} \tag{9}$$

Next, we define the function $\Gamma(x_O, v_O)$ by stating that $\Gamma(x_O, v_O)\, dx_O dv_O$ is the number of particles that cross any plane z = constant per unit depth (in y) per unit time, reach perigee within dx_O of x_O, and have perigee velocities within dv_O of v_O. Thus, the number of such particles per unit depth (y) per unit length (z) is $\frac{\Gamma}{v_g} dx_O dv_O$. Finally, using Eq. 9, we find that their contribution to the density at x is

$$d^2 n(x) = \frac{\Gamma(x_O, v_O)}{\ell_g(x_O, v_O)\, v_x(x, x_O, v_O)}\, dx_O dv_O \tag{10}$$

The total density at x is just this expression integrated between the appropriate limits.

It is somewhat easier to visualize this integration if we assume some functional relation between x_O and v_O (for example, in a monoenergetic beam). The integral becomes

$$n(x) = \int_{x_O = x_b}^{x_O = x} \frac{\Gamma(x_O)}{\ell_g(x_O)} \frac{dx_O}{v_x(x, x_O)} \tag{11}$$

where the limits are the roots of Eq. 3 solved for x_O (with v_x set to zero). These are the limits of the range of perigees of particles that are able to reach point x.

Since the potential is not known, we have to formulate the density integral for both ions and electrons, and substitute it in Poisson's equation. The possibility of a general solution has not been investigated. A simple case is discussed here.

Consider a region in which, say, only positively charged particles exist (for example, the charge sheath at the edge of the beam). Assume that they are monoenergetic,

$$\frac{1}{2} m v_O^2 + \frac{1}{2} q\phi(x_O) = H \tag{12}$$

and that the potential is quadratic,

$$\phi(x) = -\frac{1}{2} kx^2 \tag{13}$$

and hence the space-charge density is constant. Assume, also, that

$$v_O(x_O) = 0 \tag{14}$$

Since we shall show that there are, in fact, no particles reaching perigee at $x = 0$,

Eq. 14 does not imply the existence of an immobile layer of charges at $x = 0$. Thus, we have

$$n(x) = 2 \int_{x_b}^{x} \frac{\Gamma(x_o)}{\ell_g(x_o)} \frac{dx_o}{\left[\frac{qk}{m}(x^2-x_o^2) - \omega_b^2(x-x_o)^2 - 2\omega_b \frac{qk}{m} x_o(x-x_o)\right]^{1/2}} \tag{15}$$

Note that, if $\dfrac{\Gamma(x_o)}{\ell_g(x_o)}$ is constant, the integration will yield

$$n(x) = 2 \frac{\Gamma(x_o)}{\ell_g(x_o)} \frac{\pi}{(\omega_b-\omega_p)} \tag{16}$$

where we have expressed

$$\frac{qk}{m} = \frac{q}{m}\frac{dE}{dx} = \frac{q}{m}\frac{nq}{\epsilon_o} = \frac{nq^2}{m\epsilon_o} = \omega_p^2 \tag{17}$$

Since in Eq. 16 n is a constant, the solution is consistent with the assumption of a quadratic potential. We can also evaluate $\ell_g(x_o)$ by Eq. 7 to obtain

$$\ell_g(x_o) = \frac{2}{B} \int_{x=x_o}^{x=x_a} \frac{kx\,dx}{\left[\omega_p^2(x^2-x_o^2) - \omega_b^2(x-x_o)^2 - 2\omega_b\omega_p(x-x_o)x_o\right]^{1/2}} \tag{18}$$

where $x = x_a$ is the solution for $v_x(x, x_o) = 0$ with x_o held constant. This integration yields

$$\ell_g(x_o) = \frac{2k}{B} \frac{\omega_b(\omega_b-\omega_p)}{\left(\omega_b^2-\omega_p^2\right)^{3/2}} x_o = 2\left(\frac{\omega_p}{\omega_b}\right)^2 \frac{1 - \frac{\omega_p}{\omega_b}}{\left(1 - \frac{\omega_p^2}{\omega_b^2}\right)^{3/2}} x_o \tag{19}$$

so that, if Γ/ℓ_g has to be constant, $\Gamma(x_o)$ must be proportional to x_o. This implies that there are no immobile particles at the edge of the beam $(x=0)$, as we have stated. If we define the coefficient A by

$$\Gamma(x_o) = Ax_o \tag{20}$$

we can determine the curvature k of the potential by Poisson's equation,

$$n = 2 \frac{\Gamma(x_o)}{\ell_g(x_o)} \frac{\pi}{\omega_b - \omega_p} \frac{\epsilon_o k}{q} \tag{21}$$

In uniform crossed electric and magnetic fields the orbits can be visualized as a

33

(II. PLASMA DYNAMICS)

circular gyration (frequency, ω_b) superposed on an E/B drift velocity. In the case of uniform space charge, the drift velocity is E_g/B, where E_g denotes the field at the guiding center. The gyration is now elliptical, with the major axis in the drift direction. The gyration frequency is $\left(\omega_b^2 - \omega_p^2\right)^{1/2}$, which, incidentally, places a limit on the space charge, if periodic orbits are to exist. With cubic potential (linearly varying space charge), the orbits are expressible in terms of elliptic functions.

<div align="right">D. J. Rose, S. Frankenthal</div>

B. PLASMA ELECTRONICS

Prof. L. D. Smullin
Prof. A. Bers
T. J. Fessenden

1. ELECTROMAGNETIC WAVE PROPAGATION IN A PLASMA

Consider a plasma that is permeated by a uniform, time-independent, magnetic field B_{oz} in the axial direction z. In the absence of collisions, and within the framework of a first-order perturbation theory, the plasma in a magnetic field is a linear, lossless, gyroelectric medium characterized by a normalized dielectric tensor,

$$\overline{\overline{\epsilon}} = \begin{Vmatrix} \epsilon_1 & -j\epsilon_2 & 0 \\ j\epsilon_2 & \epsilon_1 & 0 \\ 0 & 0 & \epsilon_3 \end{Vmatrix} \tag{1}$$

where

$$\epsilon_1 = 1 - \frac{\tau_p^2}{1 - \tau_c^2} \qquad \tau_p = \frac{\omega_p}{\omega} \tag{2}$$

$$\epsilon_2 = \tau_c \frac{\tau_p^2}{1 - \tau_c^2} \qquad \tau_c = \frac{\omega_c}{\omega} \tag{3}$$

$$\epsilon_3 = 1 - \tau_p^2 \tag{4}$$

where ω_p is the electron plasma radian frequency, $\omega_c = -(e/m)B_{oz}$ is the electron cyclotron radian frequency, and ω is the radian frequency of the electromagnetic wave.

a. Unbounded Waves

From Maxwell's equations, the wave equation for the electric field is

$$\nabla^2 \overline{E} + \overline{\overline{K}} \cdot \overline{E} - \nabla(\nabla \cdot \overline{E}) = 0 \tag{5}$$

where

$$\overline{\overline{K}} = k^2 \overline{\overline{\epsilon}} \tag{6}$$

and $k = \omega(\mu_o \epsilon_o)^{1/2}$ is the free-space phase constant. For waves in an arbitrary direction $\overline{r}$, we assume an $\exp(-j\overline{\beta} \cdot \overline{r})$ dependence, with

$$\overline{\beta} = \overline{i}_t \beta_t + \overline{i}_z \beta_z \tag{7}$$

where $\overline{i}_z$ is a unit vector in the direction of the magnetic field B_{oz}, and $\overline{i}_t$ is a unit

vector in a plane transverse to the direction of the magnetic field B_{oz}. We then find from Eq. 7 that

$$\beta_z^4 K_3 + \beta_z^2 (K_1 + K_3) \left(\beta_t^2 - 2 \frac{K_1 K_3}{K_1 + K_3} \right) + K_1 (\beta_t^2 - K_3) \left(\beta_t^2 - \frac{K_1^2 - K_2^2}{K_1} \right) = 0 \tag{8}$$

Two cases of importance involve the purely longitudinal and purely transverse waves. In the first case, for $\beta_t = 0$, Eq. 8 gives

$$\beta_z^2 = K_1 \pm K_2 \tag{9}$$

Equation 9 represents a TEM mode that exhibits Faraday rotation. In the second case, for $\beta_z = 0$, Eq. 8 gives

$$\beta_t^2 = K_3 \tag{10}$$

and

$$\beta_t^2 = \frac{K_1^2 - K_2^2}{K_1} \tag{11}$$

Equation 10 represents a TM mode, and Eq. 11, a TE mode.

b. Bounded Waves

Consider a cylindrical system of a plasma surrounded by perfectly conducting metal walls (Fig. II-16). We assume an $\exp(-j\beta z)$ dependence (omitted hereafter) for
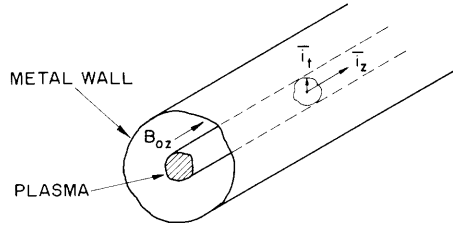

Fig. II-16. Cylindrical system of a plasma in a waveguide.

all field quantities, and we express the fields in terms of longitudinal and transverse components with respect to the magnetic field, B_{oz}.

$$\overline{E} = \overline{E}_t + \overline{i}_z E_z \tag{12}$$

$$\overline{H} = \overline{H}_t + \overline{i}_z H_z \tag{13}$$

For the space-independent dielectric tensor, Maxwell's equations give the relation between the longitudinal and transverse fields:

$$
\begin{bmatrix}
-j\beta & 0 & 0 & -j\omega\mu_o \\[4pt]
\dfrac{K_2}{\omega\mu_o} & -j\beta & \dfrac{-K_1}{j\omega\mu_o} & 0 \\[4pt]
0 & j\omega\mu_o & -j\beta & 0 \\[4pt]
\dfrac{K_1}{j\omega\mu_o} & 0 & \dfrac{K_2}{\omega\mu_o} & -j\beta
\end{bmatrix}
\begin{bmatrix}
\overline{E}_t \\[4pt]
\overline{H}_t \\[4pt]
\overline{i}_z \times \overline{E}_t \\[4pt]
\overline{i}_z \times \overline{H}_t
\end{bmatrix}
=
\begin{bmatrix}
\nabla_t E_z \\[4pt]
\nabla_t H_z \\[4pt]
\overline{i}_z \times \nabla_t E_z \\[4pt]
\overline{i}_z \times \nabla_t H_z
\end{bmatrix}
\tag{14}
$$

and also give a set of coupled wave equations for the longitudinal fields:

$$
\nabla_t^2 E_z + a E_z = b H_z \tag{15}
$$

$$
\nabla_t^2 H_z + c H_z = d E_z \tag{16}
$$

where

$$
a = \Gamma^2 \frac{K_3}{K_1} \tag{17}
$$

$$
b = -j\omega\mu_o\beta \, \frac{K_2}{K_1} \tag{18}
$$

$$
c = \Gamma^2 - \frac{K_2^2}{K_1} \tag{19}
$$

$$
d = -\frac{1}{j\omega\mu_o} \beta \, \frac{K_2 K_3}{K_1} \tag{20}
$$

and $\Gamma^2 = -\beta^2 + K_1$.

i. Uncoupled wave equations

Equations 15 and 16 show that when both b and d vanish the modes of the system can be separated into TM and TE modes. The two cases of importance are:

For $\beta = 0$: cutoff waves (see Eqs. 10 and 11).

For $K_2 = 0$: which implies any one of the three equations

$$B_{oz} = 0 \qquad K_1 = K_3 = k^2(1-\tau_p^2)$$

$$B_{oz} = \infty \qquad K_1 = k^2, \quad K_3 = k^2(1-\tau_p^2)$$

$$\omega_p = 0 \qquad K_1 = K_3 = k^2$$

The equation for $\omega_p = 0$ is trivial, since it implies an empty waveguide.

ii. Coupled wave equations

In general, for finite values of b and d (Eqs. 18 and 20), TM and TE modes cannot be identified. The solutions for the coupled wave equations involve two additional boundary conditions that can be accommodated by assuming, on the basis of linearity, that

$$E_z = e_1 + e_2 \tag{21}$$

$$H_z = h_1 e_1 + h_2 e_2 \tag{22}$$

with

$$\nabla_t^2 e_{1,2} + p_{1,2}^2 e_{1,2} = 0 \tag{23}$$

Equations 14-20 give

$$p_{1,2}^2 = \frac{1}{2}\left[-\beta^2\left(\frac{K_3}{K_1} + 1\right) + K_3 + \frac{K_1^2 - K_2^2}{K_1}\right]$$
$$\pm \frac{1}{2}\left(\left[-\beta^2\left(\frac{K_3}{K_1} - 1\right) + K_3 - \frac{K_1^2 - K_2^2}{K_1}\right]^2 + 4\beta^2 K_3 \frac{K_2^2}{K_1^2}\right)^{1/2} \tag{24}$$

which is simply the solution of Eq. 8 with $\beta_t^2 \equiv p^2$. The arbitrary constants h_1 and h_2 in Eq. 22 are

$$h_{1,2} = \frac{\left(p_{1,2}^2 - a\right)}{b} = \frac{\left(c - p_{2,1}^2\right)}{b} \tag{25}$$

The transverse fields are found to be

$$\overline{E}_t = \nabla_t(R_1 e_1 + R_2 e_2) + \overline{i}_z \times \nabla_t(S_1 e_1 + S_2 e_2) \tag{26}$$

and

$$\overline{H}_t = \nabla_t(P_1 e_1 + P_2 e_2) + \overline{i}_z \times \nabla_t(Q_1 e_1 + Q_2 e_2) \tag{27}$$

where

$$R_{1,2} = -\frac{1}{j\beta}\left(1 + \frac{K_1}{\Delta} p_{2,1}^2\right) \tag{28}$$

$$S_{1,2} = \frac{1}{\beta}\frac{K_1}{K_2}\left(1 - \frac{\Gamma^2}{\Delta} p_{2,1}^2\right) \tag{29}$$

$$P_{1,2} = \frac{1}{\omega\mu_o} \frac{K_1}{K_2} \left(1 + \frac{\Gamma^2}{\Delta} P_{2,1}^2\right) \tag{30}$$

$$Q_{1,2} = \frac{1}{j\omega\mu_o} \frac{K_1}{\Delta} P_{2,1}^2 \tag{31}$$

and $\Delta = \Gamma^2 - K_2^2$.

c. Boundary-Value Problems

As an example, we shall consider a circular waveguide partially filled with a plasma, as shown in Fig. II-17. Our immediate interest is in modes that have no ϕ-variation. Thus, we assume that

$$\frac{\partial}{\partial\phi} (\overline{E} \text{ and } \overline{H}) = 0 \tag{32}$$

The medium surrounding the plasma is assumed to be a linear, homogeneous, isotropic dielectric.

The electromagnetic fields inside the plasma are solutions of the eigenvalue problem defined by Eq. 23. The continuity of the tangential fields at r = b then gives the
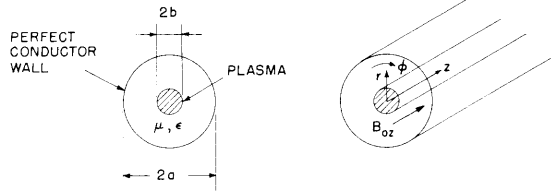

Fig. II-17. Circular waveguide partially filled with plasma.

desired determinantal equation. We summarize the results. (A superscript p will be used to denote the fields in the plasma.)

    i. Uncoupled wave equations

    For $\beta = 0$, the TM modes are given by

$$E_z^p = A_m J_o(p_m r); \quad p_m^2 = K_3 \tag{33}$$

and

$$\frac{k_a p_m}{k^2} \frac{J_1(p_m b)}{J_o(p_m b)} = \frac{\epsilon}{\epsilon_o} \frac{H_{o,1}}{H_{o,o}} \tag{34}$$

The TE modes are given by

$$H_z^p = A_e J_0(p_e r); \qquad p_e^2 = \frac{K_1^2 - K_2^2}{K_1} \tag{35}$$

and

$$\frac{k_a}{p_e} \frac{J_1(p_a b)}{J_0(p_a b)} = \frac{\mu}{\mu_0} \frac{H_{1,1}}{H_{1,o}} \tag{36}$$

where

$$H_{mn}(x, y) = \frac{\pi}{2} \left[J_m(x) N_n(y) - N_m(x) J_n(y) \right]; \qquad x = \gamma_a, \; y = \gamma_b \tag{37}$$

is the biradial function (2); $J_0(x)$ and $J_1(x)$ are the Bessel functions of the first kind; $N_0(x)$ and $N_1(x)$ are the Neumann functions; and $k_a^2 = \omega^2 \mu \epsilon$.

For $K_2 = 0$, the TM modes are given by

$$E_z^p = A_m J_0(p_m r); \qquad p_m^2 = \Gamma^2 \frac{K_3}{K_1} \tag{38}$$

and

$$\frac{K_1}{k^2} \frac{\gamma p_m}{\Gamma^2} \frac{J_1(p_m b)}{J_0(p_m b)} = \frac{\epsilon}{\epsilon_0} \frac{H_{o,1}}{H_{o,o}} \tag{39}$$

The TE modes are given by

$$H_z^p = A_e J_0(p_e r); \qquad p_e^2 = \Gamma^2 \tag{40}$$

and

$$\frac{\gamma p_e}{\Gamma^2} \frac{J_1(p_e b)}{J_0(p_e b)} = \frac{\mu}{\mu_0} \frac{H_{1,1}}{H_{1,o}} \tag{41}$$

where $\gamma^2 = -\beta^2 + k^2$.

ii. Coupled wave equations

The solution of Eq. 23 gives

$$E_z^p = A_1 J_0(p_1 r) + A_2 J_0(p_2 r) \tag{42}$$

where $p_{1,2}^2$ are related to β by Eq. 24. The boundary conditions at $r = b$ give

$$D_1 T_2 - D_2 T_1 = 0 \tag{43}$$

where

$$D_{1,2} = -\frac{j\omega\mu}{\gamma} \frac{H_{1,1}}{H_{1,0}} h_{1,2} J_0(p_{1,2}b) + S_{1,2} p_{1,2} J_1(p_{1,2}b) \qquad (44)$$

$$T_{1,2} = \frac{j\omega\epsilon}{\gamma} \frac{H_{0,1}}{H_{0,0}} J_0(p_{1,2}b) + Q_{1,2} p_{1,2} J_1(p_{1,2}b) \qquad (45)$$

In general, Eqs. 33-45 must be solved numerically for p_e, p_m, $p_{1,2}$, and β. The study of simple cases of special interest will continue.

A. Bers

References

1. A. A. Th. M. Van Trier, Guided electromagnetic waves in anisotropic media, Appl. Sci. Res., Sec. B, Vol. 3, p. 305 (1953).

2. C. K. Birdsall, et al., Biradial functions useful in boundary value problems, Internal Memorandum, General Electric Microwave Laboratory, Palo Alto, California, 1953.

C. PLASMA MAGNETOHYDRODYNAMICS[*]

Prof. O. K. Mawardi
Prof. D. O. Akhurst
Prof. D. C. Pridmore-Brown
Prof. J. L. Smith, Jr.

Prof. H. H. Woodson
Dr. I. C. T. Nisbet
D. A. East

A. T. Lewis
J. K. Oddson
M. J. Pollock
Z. J. J. Stekly

1. HYDROMAGNETIC WAVEGUIDE

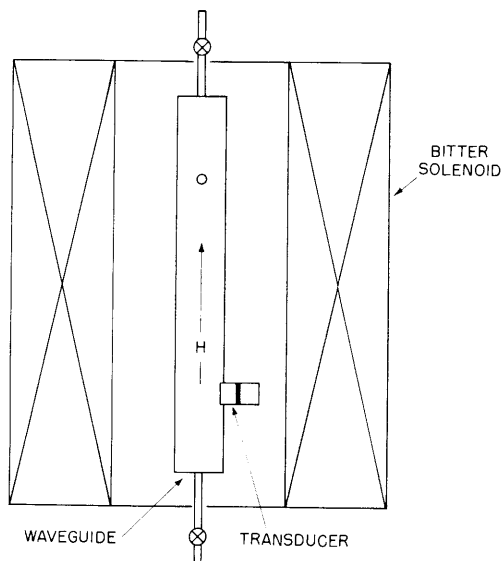A series of measurements was performed to test the theory of the hydromagnetic waveguide that was described in Quarterly Progress Report No. 51, pages 23-26. The waveguide consists of a copper conduit of rectangular cross section, approximately 1 foot long. A sandwich transducer has been attached to one side of the conduit (Fig. II-18). The transducer induces a perturbation in the fluid, with the result that the mass motion is at right angles to the magnetic lines of force. This, in turn, leads to hydromagnetic waves that propagate along the axis of the waveguide.

Fig. II-18. Schematic diagram for the alignment of the waveguide inside the electromagnet.

The hydromagnetic waves are detected by a probe that measures the electric field at right angles to the mass motion and to the lines of force.

Preliminary measurements have been carried out for field strengths up to 48,000 gauss. The transducer is excited at 12 kc and modulated by 10-msec square pulses at a repetition rate of 25 cps.

The measurements indicate substantial agreement with the theory previously discussed.

M. J. Pollock, O. K. Mawardi

2. HYDROMAGNETIC SHOCKS

The shock motion in an electric shock tube, the driving current of which is known, and in which the shock propagates into a region of constant magnetic field, is best
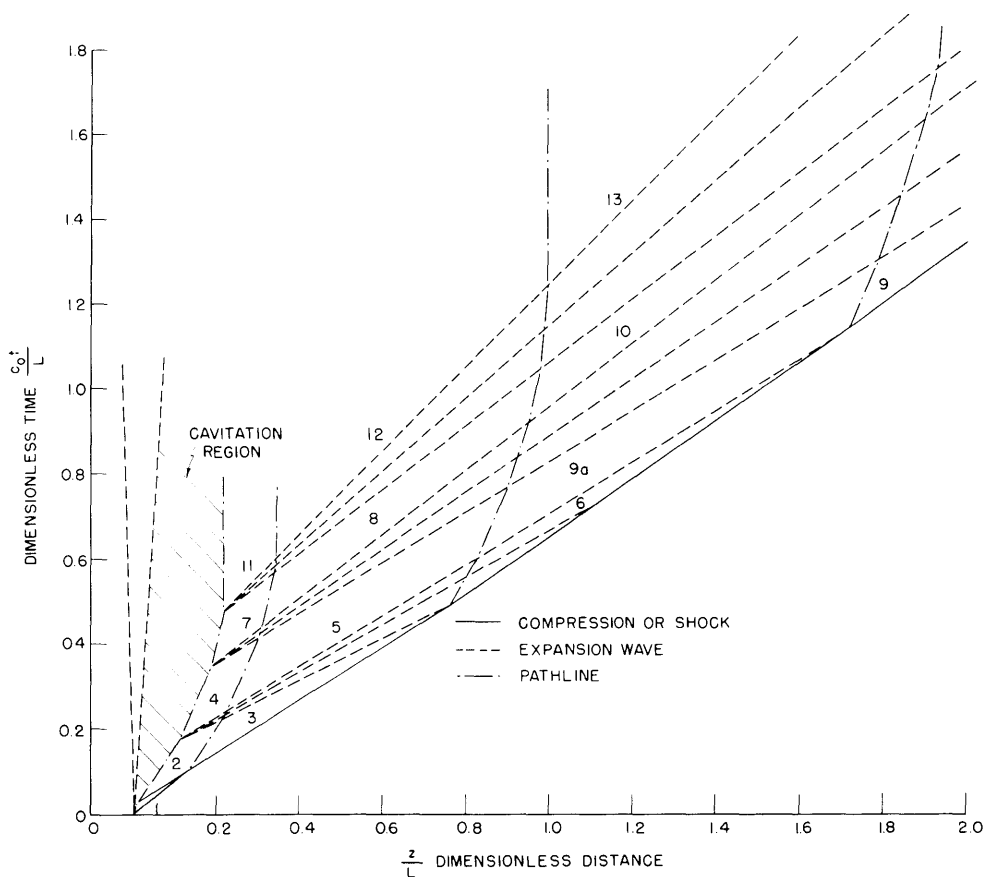
42

Fig. II-19. Wave diagram for hydromagnetic shock tube.

understood by constructing the wave diagram shown in Fig. II-19.

This construction makes use of the governing equations for the motion of a hydro-magnetic shock, discussed in previous reports (1,2). These equations have been reworked in a more convenient form, as follows.

$$\frac{u_s}{c_o} = \left(\frac{1 + s_o + \frac{2-\gamma}{2}\left(\frac{\rho_1}{\rho_o}-1\right)}{(1+s_o)\left[1 - \frac{\gamma-1}{2}\left(\frac{\rho_1}{\rho_o}-1\right)\right]} \left(\frac{\rho_1}{\rho_o}\right) \right)^{1/2} \tag{1}$$

$$\frac{s_1}{s_o} = \left[1 + \frac{\gamma\left(\frac{\rho_1}{\rho_o}-1\right)\left[1 + \frac{\gamma-1}{4s_o}\left(\frac{\rho_1}{\rho_o}-1\right)^2\right]}{1 - \frac{\gamma-1}{2}\left(\frac{\rho_1}{\rho_o}-1\right)} \right] \frac{\rho_o^2}{\rho_1^2} \tag{2}$$

$$\frac{c_1}{c_o} = \left(\frac{\rho_1}{\rho_o} \frac{1 + s_o \left(\frac{s_1}{s_o}\right)}{1 + s_o} \right)^{1/2} \tag{3}$$

$$\frac{p_1^*}{p_o^*} = \frac{p_1 + \frac{B_1^2}{2\mu_o}}{p_o + \frac{B_o^2}{2\mu_o}} = \frac{\left(1 + \frac{\gamma}{2s_o} \cdot \frac{s_o}{s_1}\right)}{1 + \frac{\gamma}{2s_o}} \left[1 + \frac{\gamma\left(\frac{\rho_1}{\rho_o} - 1\right)\left[1 + \frac{\gamma - 1}{4s_o}\left(\frac{\rho_1}{\rho_o} - 1\right)^2\right]}{1 - \frac{\gamma - 1}{2}\left(\frac{\rho_1}{\rho_o} - 1\right)} \right] \tag{4}$$

$$\frac{u_1 - u_o}{c_o} = \left(\frac{1 + s_o + \left(\frac{2-\gamma}{2}\right)\left(\frac{\rho_1}{\rho_o} - 1\right)}{(1+s_o)\left[1 - \frac{\gamma - 1}{2}\left(\frac{\rho_1}{\rho_o} - 1\right)\right]} \right)^{1/2} \left[\left(\frac{\rho_1}{\rho_o}\right)^{1/2} - \left(\frac{\rho_o}{\rho_1}\right)^{1/2} \right] \tag{5}$$

In expressions 1-5: u_s stands for the shock velocity with respect to the fluid ahead of it; $c_{o,\,1}$, for the characteristic velocity of propagation ahead of and behind the shock;
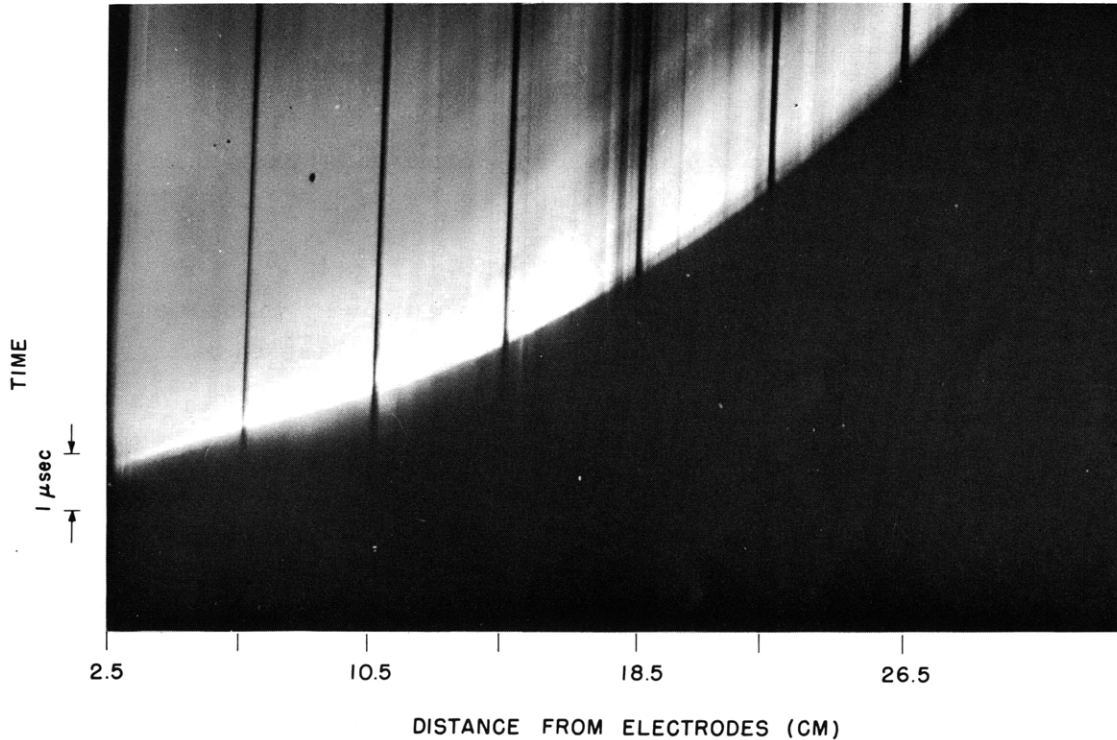

Fig. II-20. Smear camera photograph for shock predicted in Fig. II-19. Magnetic field, 0.373 webers/m^2; pressure, 0.5 mm Hg; capacitive discharge voltage, 16.5 kv.
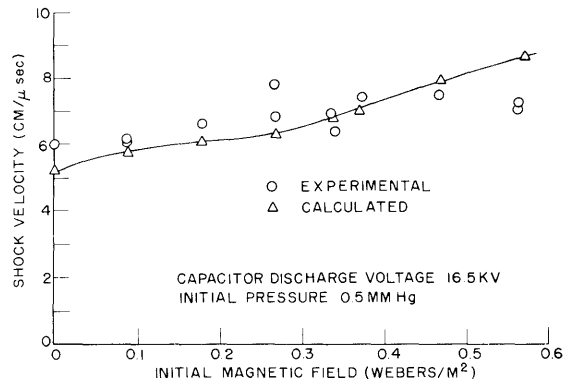
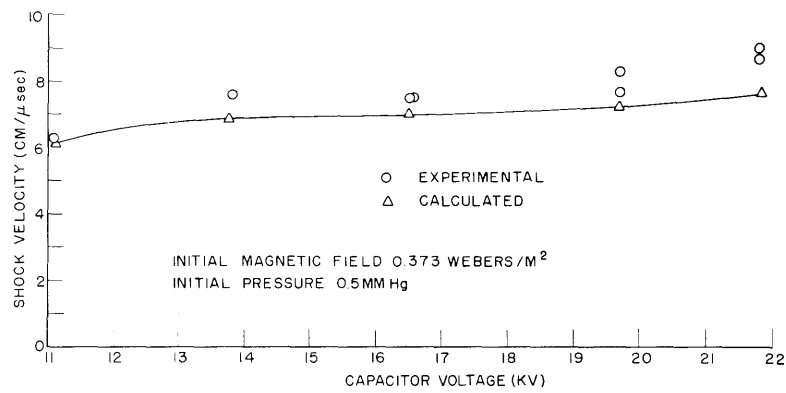Fig. II-21. Maximum shock velocity versus initial magnetic field.

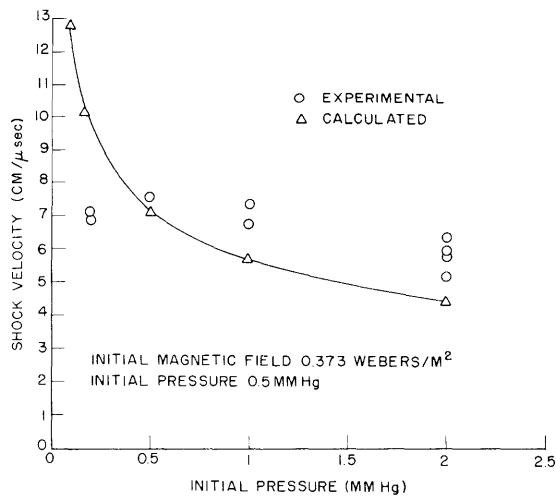Fig. II-22. Maximum shock velocity versus initial capacitor voltage.

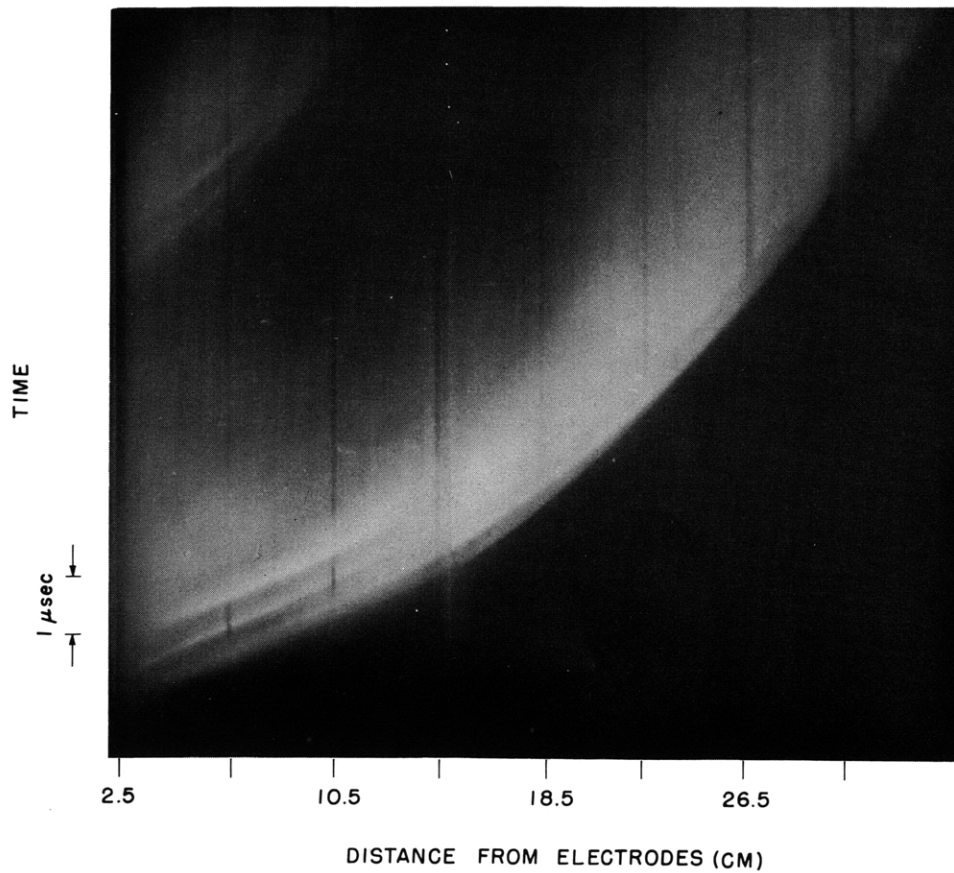Fig. II-23. Maximum shock velocity versus initial pressure.

45

TIME

I μsec

2.5   IO.5   I8.5   26.5

DISTANCE FROM ELECTRODES (CM)

Fig. II-24.   Smear camera photograph showing three successive shocks. Magnetic field, 0.373 webers/m^2; pressure, 0.5 mm Hg; capacitors' discharge voltage, 12.5 kv.
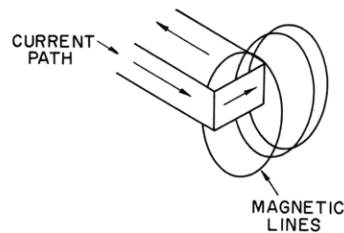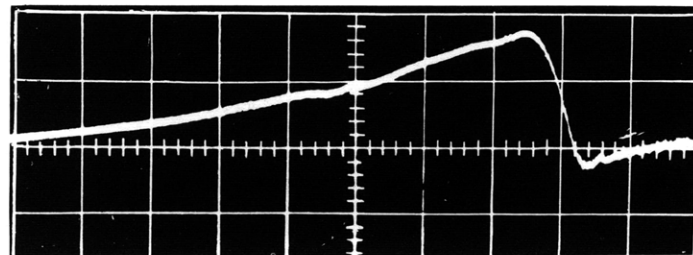

CURRENT PATH

MAGNETIC LINES

Fig. II-25.   Probe measurement of the magnetic field profile in the vicinity of the shock. The shock moves from left to right. The small dip ahead of the shock is caused by the return path of the lines of force, as indicated in the accompanying sketch.

$u_{o, 1}$, for the velocity ahead and behind the shock; $p^*_{o, 1}$, for the total pressure (sum of particle and magnetic pressure); $s_{o, 1}$, for the ratio of the speed of sound squared to the Alfvén velocity squared; $\rho_{o, 1}$, for the density ahead of and behind the shock; and γ, for the ratio of specific heats.

When the density ratio, ρ_1/ρ_0 is eliminated from Eqs. 1-5, and the ratios p^*_1/p^*_o, c_1/c_0 are plotted against $(u_1 - u_0)/c_0$, the curves depend very slightly on the parameter s_0. If the total pressure p^* and the characteristic velocity

$$c = \frac{\gamma p}{\rho} + \frac{B^2}{\mu_o \rho}$$

are used, the governing equations for the hydromagnetic shock moving in a transverse field become analogous to those for a conventional gas dynamic shock.

As the current increases, the compression waves are generated. These eventually steepen into a shock wave. Conversely, a decreasing current generates expansion waves that catch up with the shock and slow it down. We note from Fig. II-19 that the shock front first accelerates, then decelerates as the expansion waves catch up with it. This is corroborated by experiment, as shown in the smear camera photograph (Fig. II-20).

The maximum shock velocity for any given set of conditions can be calculated from Eqs. 1-5. Comparison of experiment and theory is presented in Figs. II-21, II-22, and II-23. Agreement is seen to be good, except at very low pressures, at which the losses to the wall and surroundings become excessive.

The back emf caused by the motion of the shock wave through a magnetic field increases as the velocity of the shock wave increases. At low initial capacitor voltages, the voltage applied to the electrodes may be less than that required to overcome the back emf. In this case, the driving current sheet may be extinguished, and the arc strikes again elsewhere in the gas. This phenomenon is clearly shown in Fig. II-24, in which the formation of three successive shock waves is shown.

Measurement of the transient magnetic field is made by inserting a small probe into the shock tube on its axis. A typical oscillogram obtained in this way is shown in Fig. II-25.

<div align="right">Z. J. J. Stekly, O. K. Mawardi</div>

References

1. O. K. Mawardi and Z. J. J. Stekly, Studies of magnetohydrodynamic shocks, Quarterly Progress Report No. 51, Research Laboratory of Electronics, M.I.T., Oct. 15, 1958, pp. 27-28.

2. Ibid., Quarterly Progress Report No. 52, Jan. 15, 1959, pp. 20-21.